What Causes Weak Orographic Rain Shadows? Insights from Case Studies in the Cascades and Idealized Simulations

NICHOLAS SILER[a] AND DALE DURRAN

Department of Atmospheric Sciences, University of Washington, Seattle, Washington

(Manuscript received 14 December 2015, in final form 15 July 2016)

ABSTRACT

Recent studies have shown that weak rain shadows in the Cascade Mountains are associated with passing warm fronts, but the specific mechanisms responsible for this connection have eluded consensus. One theory holds that weak rain shadows are the result of enhanced precipitation over eastern slopes caused by easterly upslope flow; the other suggests that condensation is produced primarily over the western slopes, with enhanced east-slope precipitation occurring in dynamical regimes that minimize descent and evaporation east of the crest. Here these mechanisms are investigated through numerical simulations involving both real and idealized topography. Consistent with the second theory, storms with weak rain shadows are found to exhibit much weaker mountain waves in the lee of the Cascades than storms with strong rain shadows, with correspondingly weaker leeside evaporation. The muted wave activity during weak-rain-shadow storms is found to be caused by cold, zonally stagnant air at low levels in the lee, which precedes the warm front, and remains in place as the progression of the front is impeded by the mountains. As the front brings warmer air aloft, the static stability of the zonally stagnant layer increases, making it more resistant to erosion by the overlying flow. This in turn allows the weak rain shadow to persist long after the front has passed. If the midlatitude storm tracks shift poleward in a warmer climate, the results suggest there could be an increase in the strength of the rain shadow in mountainous regions astride the current storm tracks.

1. Introduction

Like many midlatitude mountain ranges, Washington State's Cascade Mountains exhibit a strong orographic rain shadow, with much wetter western slopes than eastern slopes as a result of prevailing westerly flow during the winter storm season. As recent studies have observed, however, the magnitude of the rain-shadow effect varies significantly from storm to storm and from year to year (Leung et al. 2004; Siler et al. 2013). Such variability can have significant consequences for the region's streams and rivers, which provide crop irrigation, hydroelectric power, spawning habitat for salmon, and drinking water to several million people. These impacts are especially pronounced in eastern watersheds, where water is most limited, and where much of the state's agriculture industry and hydroelectric capacity is located.

In the past few years, two studies have addressed the physical mechanisms governing rain-shadow variability in the Cascades. In the first study, Siler et al. (2013) found that around 70% of interannual variability in the strength of the wintertime rain shadow could be explained by fluctuations in the large-scale atmospheric circulation, caused in part by the El Niño–Southern Oscillation (ENSO). On shorter time scales, the authors analyzed 100 storms between 2005 and 2010 and found that storms with unusually weak rain shadows [called weak-rain-shadow (WRS) storms] tended to be associated with the passage of warm or occluded fronts over the Cascades. In contrast, strong-rain-shadow (SRS) storms tended to exhibit little temperature advection over the Cascades, with precipitation occurring primarily within the storms' warm sectors. Two case studies of individual WRS and SRS storms revealed significant differences in mountain-wave activity, particularly in the lee of the mountain range. In the SRS case, precipitation over the eastern slope was inhibited by strong

[a] Current affiliation: Scripps Institution of Oceanography, University of California, San Diego, La Jolla, California.

Corresponding author address: Nicholas Siler, Scripps Institution of Oceanography, University of California, San Diego, 9500 Gilman Drive, #0206, La Jolla, CA 92093-0206.
E-mail: nsiler@ucsd.edu

DOI: 10.1175/JAS-D-15-0371.1

wave-induced descent, while in the WRS case, wave activity was weaker, and precipitation was distributed more evenly across the range.

More recently, Mass et al. (2015) analyzed the synoptic conditions favorable to weak or strong rain shadows by comparing hourly rain gauge data from a few low-elevation sites east and west of the Cascades. Like Siler et al. (2013), they found that weak rain shadows tend to coincide with the passage of warm or occluded fronts through the region. According to their analysis, the weakest rain shadows (with eastern precipitation exceeding western precipitation) occur prior to the passage of warm or occluded fronts, when winds at low levels have a significant easterly component. This is thought to cause ascent and condensation over eastern slopes and descent and evaporation over western slopes, effectively reversing the climatological rain shadow. In other instances of warm or occluded frontal passage, winds were found to be southerly at low levels, resulting in minimal orographic influence and roughly equal amounts of precipitation east and west of the Cascades. However, both types of WRS scenarios were found to be quite rare, occurring in only 5% of the hour-long time periods during which precipitation fell in the region. The rest of the time, winds tended to be westerly or southwesterly throughout the region, resulting in significantly wetter conditions at western sites than at eastern sites, indicative of a strong rain shadow.

Together, the results of Siler et al. (2013) and Mass et al. (2015) make a convincing case that warm-air advection, accompanied by southerly or southeasterly flow at low levels, is strongly associated with the occurrence of unusually weak rain shadows in the Cascades. Beyond this general result, however, the two studies offer rather different interpretations of the specific dynamical mechanisms responsible for weak rain shadows. In the WRS storm analyzed by Siler et al. east-slope precipitation was thought to result primarily from clouds and precipitation carried over the crest from the west, while the absence of vigorous wave-induced descent prevented it from evaporating before reaching the lee slope. On the other hand, the results of Mass et al. suggest a greater role for eastern sources of condensation, resulting either from frontal dynamics or from upslope ascent associated with low-level easterly winds.

The purpose of this paper is to develop a clearer understanding of the mechanisms responsible for east-slope precipitation during WRS storms. We begin in section 2 by analyzing numerical simulations of several WRS and SRS storms, focusing on the 6 h of each storm during which the greatest precipitation fell over the Cascades. In all storms, we find that condensation is greatest over western slopes and that eastern sources of condensation, while present to varying degrees in WRS storms, contribute less than half of the storm-total precipitation east of the crest. Consistent with the hypothesis of Siler et al. (2013), we find that WRS storms are characterized by much weaker mountain waves in the lee of the range than their SRS counterparts, with correspondingly weaker leeside evaporation. A comparison of the wind and stability profiles of WRS and SRS storms suggests that muted wave activity during WRS storms is caused by the presence of stagnant, stable air at low levels in the lee, which is absent in SRS storms. Further evidence in support of this hypothesis is presented in section 3, based on two-dimensional simulations involving a stagnant, stable layer in the lee of an idealized ridge. In section 4, we examine the origin and evolution of this layer during warm-frontal passage, using a simulation of a real WRS storm, but with the Cascades replaced by idealized topography. In section 5, the preceding results are synthesized in a schematic illustration of the evolution of the rain shadow during a warm-frontal passage. Section 6 contains the conclusions.

2. Case studies

a. Methods

Our case studies are chosen from the same set of the 100 strongest storms in 6 years of archived forecast-model output for the years 2005–10 described in Siler et al. (2013). As in the previous study, these storms were sorted according to their rain-shadow index, which was calculated by normalizing the time series of precipitation over western and eastern slopes independently, then taking their difference. Our present analysis will focus on three WRS and three SRS storms, each of which ranked in the top 10 of weakest- or strongest-rain-shadow storms within the 100-storm dataset. These six storms—which include the two case studies discussed in Siler et al. (2013)—were chosen to reflect the synoptic diversity found among storms of each type, as will be discussed further in section 2b.

Simulations were performed using version 3.5.1 of the Weather Research and Forecasting (WRF) Model, with initial and boundary conditions supplied by the National Centers for Environmental Prediction (NCEP) Global Forecast System (GFS) analysis. The model domain consisted of four nested grids with 38 vertical levels and horizontal resolutions of 36, 12, 4, and 4/3 km, centered over the Washington Cascades (Fig. 1a). The

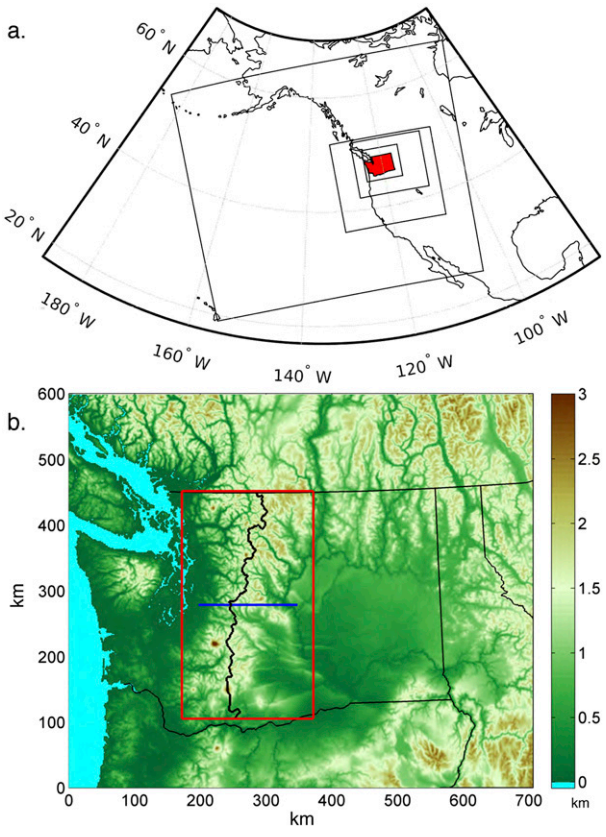

FIG. 1. (a) The boundaries of the four nested grids used in each WRF simulation. (b) The innermost grid, with colors representing terrain elevation (km). For the purposes of our analysis, we define the Washington Cascades to be the region inside the red box. The black line represents the crest, and the blue line represents a 150-km transect through the center of the Washington Cascades, along which vertical cross sections are shown in Figs. 6 and 7.

innermost grid (Fig. 1b) spanned 531 grid points (~700 km) east–west and 450 grid points (~600 km) north–south. The model was run with the same configuration (current as of December 2014) used by the Northwest Modeling Consortium to perform operational forecasts twice daily over the Pacific Northwest. However, in order to shed light on the source of east-slope precipitation, we have programmed the model to output the water-vapor tendency at each time step, which we then use to calculate the column-integrated rate of condensation (or evaporation). Physical parameterizations used in the model include the microphysics scheme of Thompson et al. (2008), the updated planetary boundary layer scheme from Yonsei University (Hong 2010), and the Noah-MP land surface model (Niu et al. 2011). Further details can be found in the change log and sample namelist file available on the consortium's website, http://www.atmos.washington.edu/mm5rt/info.html.

TABLE 1. (first column) Storm abbreviations, (second column) dates, (third column) domain-averaged 6-h precipitation over the Washington Cascades (in.), and (fourth column) ratios of western to eastern precipitation. Dates represent the beginning of the 6-h period of peak precipitation.

	Date	P_{avg}	P_{west}/P_{east}
WRS storms			
W1	0800 UTC 30 Dec 2005	0.65	0.81
W2	0200 UTC 1 Feb 2006	0.45	1.23
W3	2000 UTC 14 Dec 2006	0.74	1.24
SRS storms			
S1	0000 UTC 7 Nov 2006	0.90	2.39
S2	1200 UTC 3 Dec 2007	0.62	1.82
S3	1000 UTC 12 Nov 2008	0.78	1.97

The simulations were initialized at least 18 h before each storm fully impacted the Washington Cascades. Boundary conditions for the outermost grid were updated every 6 h with GFS output, and the simulations were allowed to run continuously for 48 h, by which time precipitation from each storm had largely passed. Our analysis below focuses on the 6-h period of each simulation during which the most precipitation fell in the Washington Cascades, defined for our purposes as the region inside the red box in Fig. 1b. Table 1 lists the date and time of each storm, its 6-h maximum precipitation, and the ratio of precipitation that fell on western slopes versus eastern slopes, which serves as a rough indicator of rain-shadow strength.[1] For simplicity, we will refer to each storm by its one-letter rain-shadow classification (W for WRS storms, S for SRS storms), followed by a number representing its chronological order (1, 2, or 3), as listed in Table 1.

b. Analysis

We begin with a discussion of the synoptic conditions present during each storm. Figure 2 shows sea level pressure (SLP, black contours) and the thickness of the layer between 1000 and 850 hPa at the beginning of each storm's 6-h window. The thickness field is proportional to lower-tropospheric temperature, so strong gradients are indicative of fronts. Among the storms in each category, significant differences are evident in the location of the low-pressure center and the orientation of the isobars in the vicinity of the Cascades. Indeed, the storms were chosen specifically to capture the wide range of synoptic conditions found within the larger

[1] Note that the rain-shadow index according to which these storms were ranked in the top 10 strongest or weakest rain-shadow events was computed from normalized windward and leeward precipitation differences, not from this simple ratio.

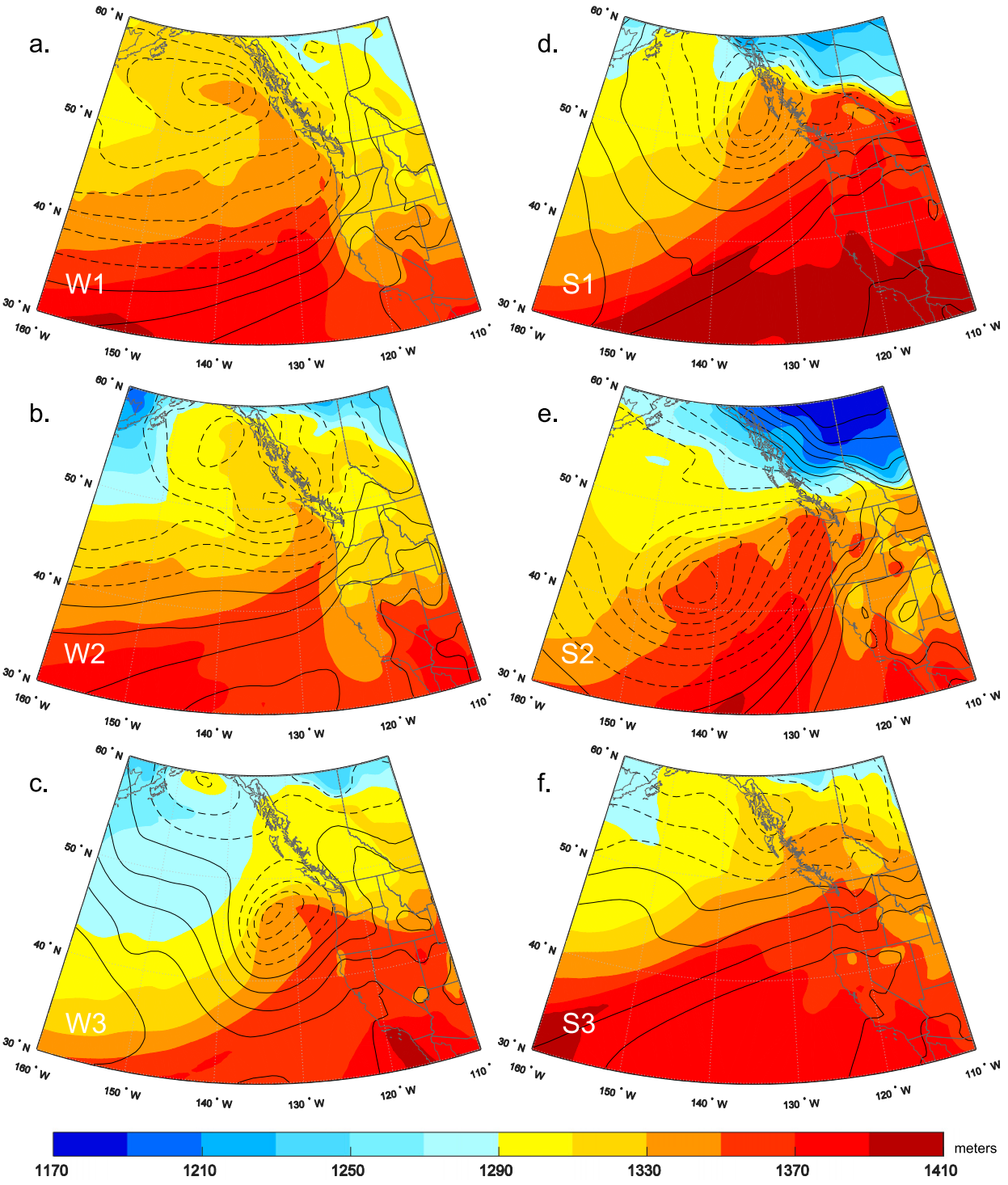

FIG. 2. Sea level pressure (black contours at 6-hPa intervals, dashed for values less than or equal to 1000 hPa) and 1000–850-hPa thickness (colors; m) at the beginning of each storm's 6-h period of maximum precipitation, based on ERA-Interim. (a) W1. (b) W2. (c) W3. (d) S1. (e) S2. (f) S3.

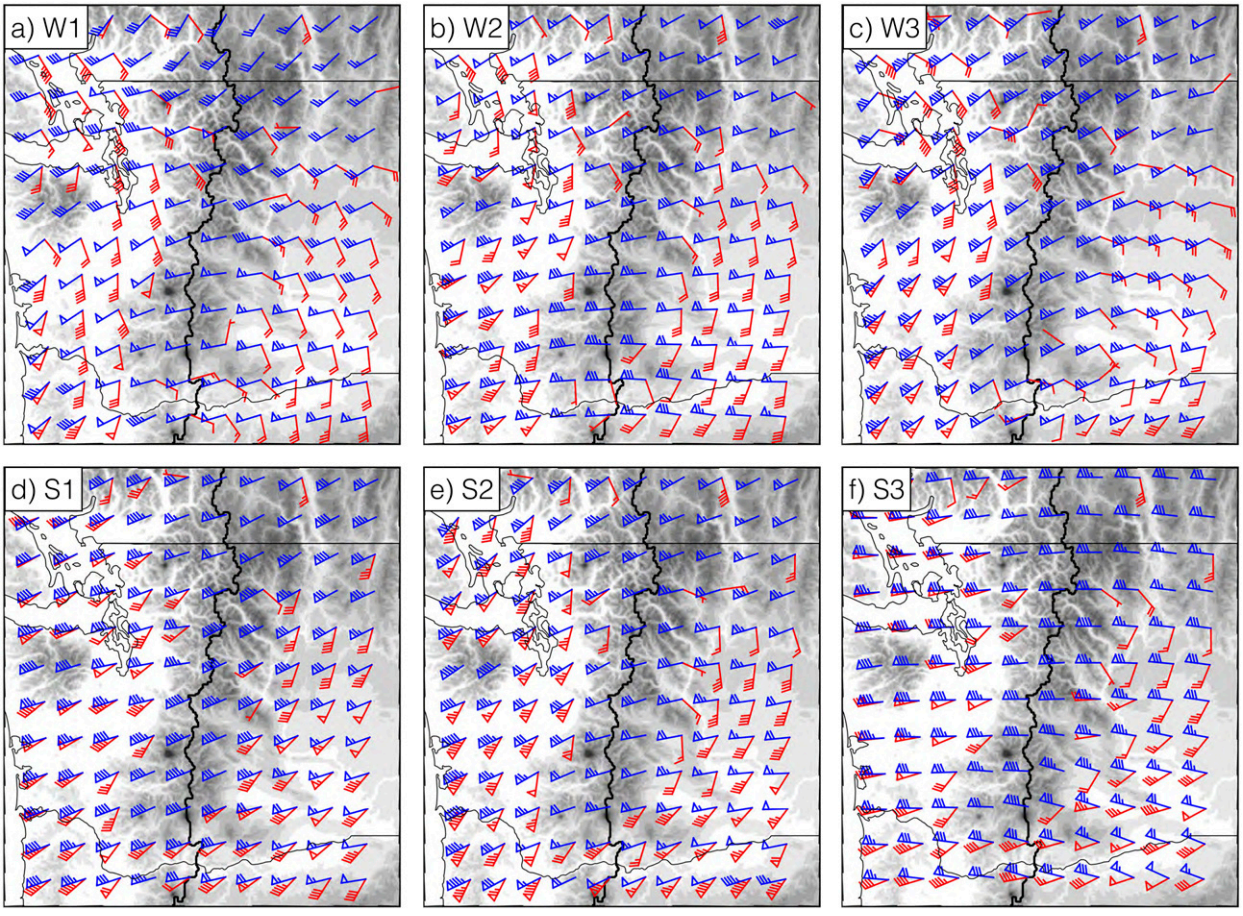

FIG. 3. Wind barbs [knots (kt; 1 kt = 0.51 m s^{-1})] at 1 (red) and 5 km (blue) above sea level at the beginning of the 6-h period of maximum precipitation of storms with (top) weak and (bottom) strong rain shadows. Terrain elevation is shaded in gray, while the thick black line represents the Cascade crest. (a) W1. (b) W2. (c) W3. (d) S1. (e) S2. (f) S3.

subsets of WRS and SRS storms. Despite these differences, however, the synoptic conditions during each storm are consistent with the canonical picture presented by Siler et al. (2013): in each WRS storm, a warm or partially occluded front approached the Cascades from offshore, while in each SRS storm, the Cascades lay within the warm sector, where there was little warm-air advection.

Horizontal winds provide further evidence of differences in warm-air advection between SRS and WRS storms. Figure 3 shows wind barbs at 1 (red) and 5 km (blue) above sea level at the beginning of each storm's 6-h window, with elevation shaded in gray. As expected with stronger warm-air advection, the WRS storms exhibit more veering (i.e., clockwise turning) with height. For example, veering between 1- and 5-km averages[2] 92°, 71°, and 84° in each of the WRS storms, but only 29°, 50°, and 39° in the SRS storms. This contrast in veering is due almost entirely to differences in wind direction at 1 km, which averages 163° (southeasterly) across WRS storms and 217° (southwesterly) across SRS storms—a difference of 54°. By comparison, the average wind direction at 5 km differs by only 11° between WRS and SRS storms (246° vs 257°).

What is the role of wind direction in regulating the strength of the rain shadow? One possibility, discussed by Mass et al. (2015), is that southeasterly flow at low levels during WRS storms enhances condensation as it rises over the eastern slopes of the Cascades, causing a reversal of the climatological rain shadow. If this played a significant role during WRS storms, we might expect to see evidence of enhanced condensation and precipitation along the eastern slope, as well as net evaporation along the western slope. In reality, however, spatial patterns of precipitation (Fig. 4) and condensation (Fig. 5) show little evidence of either effect.

[2] This average includes all grid points within the domain of Fig. 3 where the height of the topography is less than 1 km.

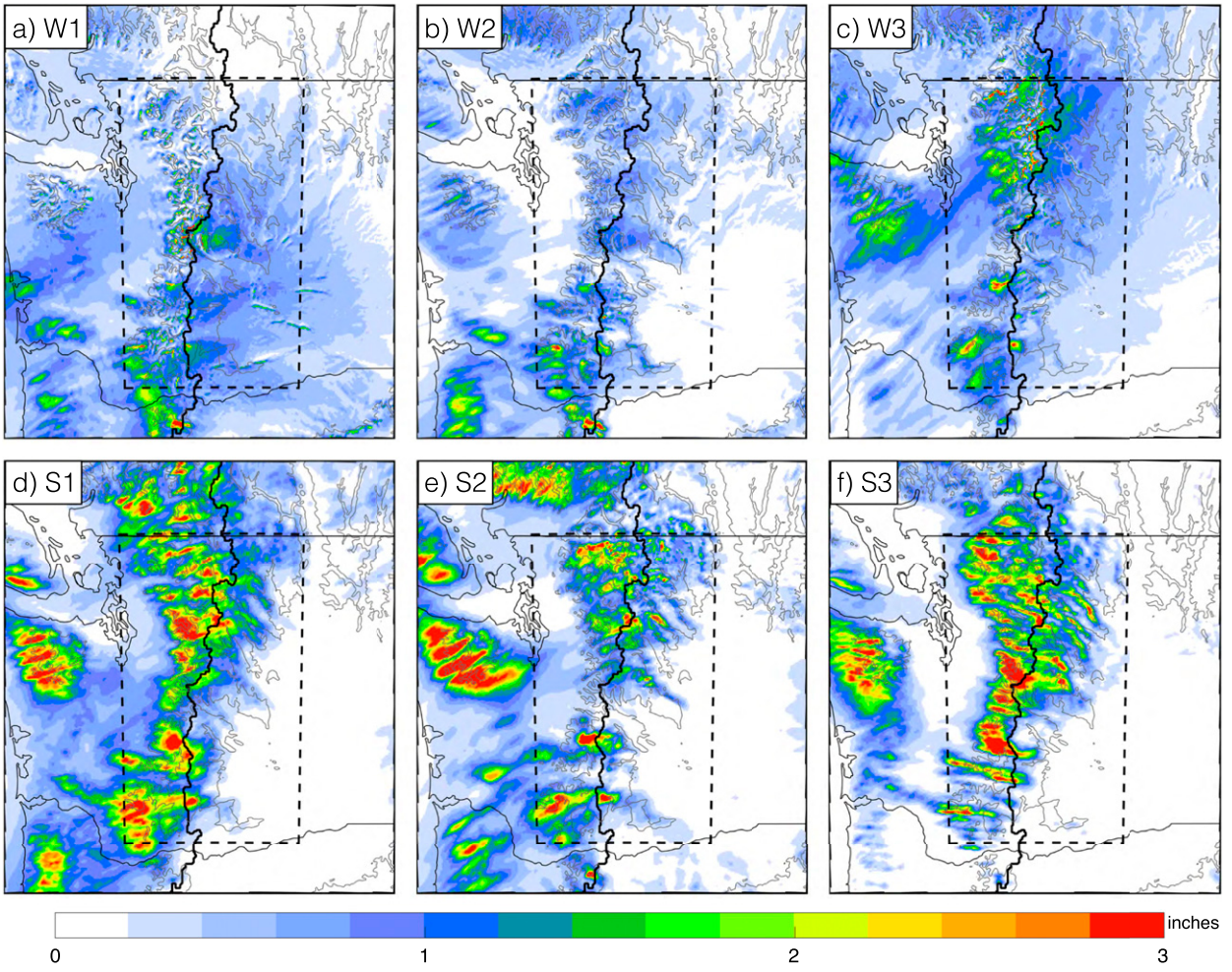

FIG. 4. Total precipitation (in.) during the 6-h period of maximum precipitation of each storm. The gray contour represents 1-km elevation. The solid black line represents the Cascade crest, and the dashed black line represents the Washington Cascades region, over which the precipitation totals in Table 1 were calculated. (a) W1. (b) W2. (c) W3. (d) S1. (e) S2. (f) S3.

As a further test of this hypothesis, we have calculated the net flux of water vapor across the crest during each storm's 6-h period of maximum precipitation (see appendix), as shown in the second column of Table 2. While the cross-crest flux is generally weaker during WRS storms than during SRS storms, it is still westerly in each case, contrary to what one would expect with a reversal of the climatological rain shadow.

An alternative theory, also put forth by Mass et al. (2015), is that stronger veering during WRS storms minimizes the influence of the mountains altogether, such that condensation and precipitation are essentially governed by large-scale dynamics. However, two pieces of evidence suggest that this is not the case. First, in every WRS storm, precipitation over eastern slopes significantly exceeds net condensation over eastern slopes (fourth and fifth columns of Table 2). In fact, with only one exception (W1), much more condensate is advected over the crest from the west than is generated locally by condensation (third vs fourth columns of Table 2), implying that orographic "spillover" is an important source of east-slope precipitation during WRS storms.

Second, the drying ratios of WRS storms further challenge the theory of weak orographic influence (sixth column of Table 2). The drying ratio is defined as the fraction of upstream moisture flux that precipitates over a mountain range, and it is often interpreted as a measure of the degree of orographic precipitation enhancement (e.g., Smith 2006). To calculate the drying ratio for each storm, we divide the total precipitation over the Cascade region (defined by the area inside the dashed black box in Figs. 4 and 5) by the total moisture flux through the western and southern boundaries of the

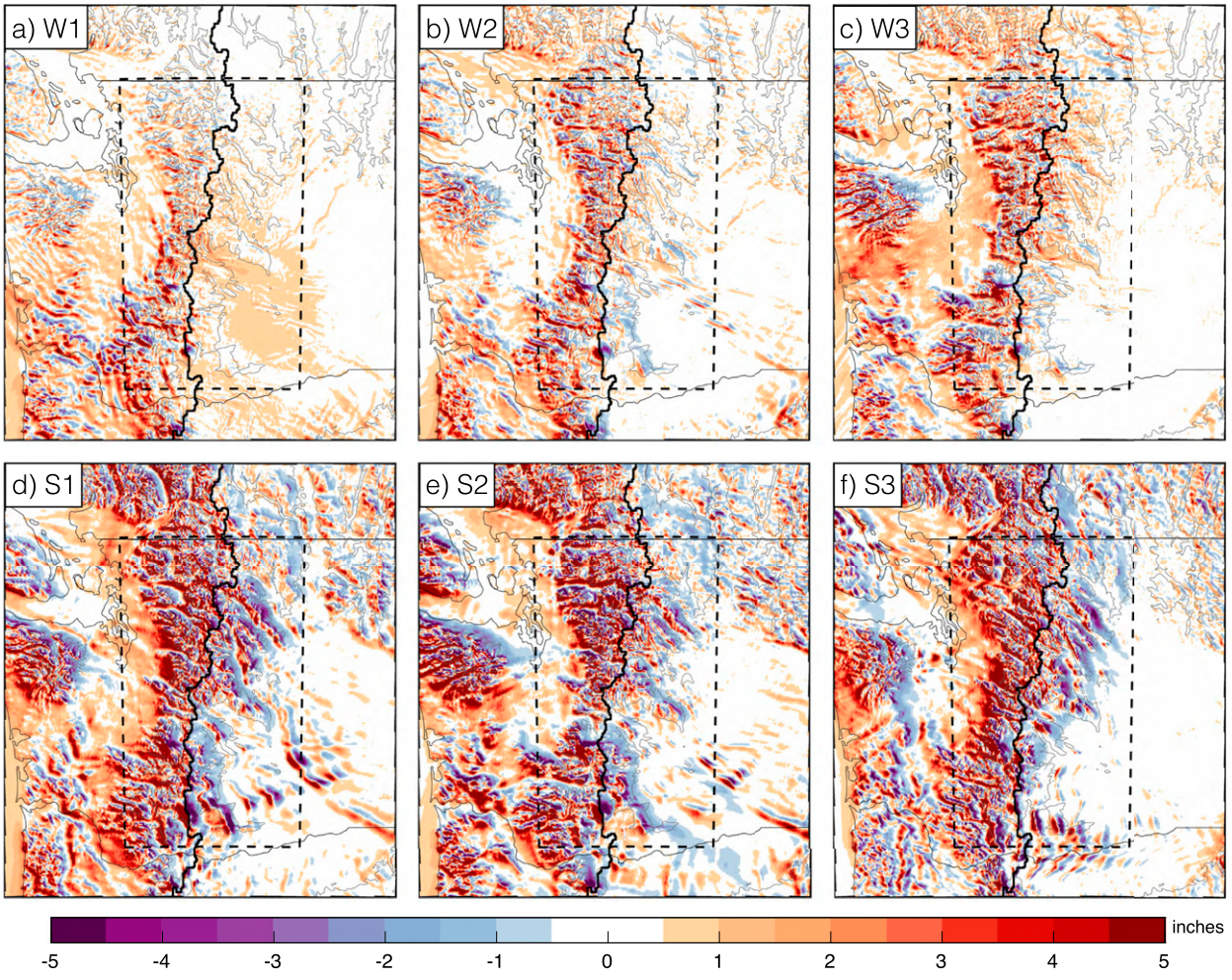

FIG. 5. As in Fig. 4, but for column-integrated condensation (in.). Negative values denote net evaporation.

same region.[3] The ratio was calculated every 2 h and then averaged over each storm's 6-h period of maximum precipitation. Comparing the drying ratios of WRS and SRS storms in Table 2, we find consistently larger values in the former case, suggesting, if anything, more orographic enhancement during WRS storms than during SRS storms.

Based on these observations, therefore, it does not appear that orography per se plays less of a role during WRS storms than during SRS storms. Instead, the main contrast between WRS and SRS storms occurs in the lee, where WRS storms exhibit net condensation while SRS storms exhibit net evaporation (fourth column of Table 2). During WRS storms, the absence of leeside evaporation allows clouds and hydrometeors generated over western slopes to remain intact as they spill over the crest, significantly enhancing precipitation over the eastern slopes. On the other hand, during SRS storms, vigorous leeside evaporation suppresses all precipitation beyond 10 or 20 km east of the crest (Figs. 4d–f).

Considering that evaporation is typically associated with descending air, one might guess that the contrast in east-slope evaporation between WRS and SRS storms would be related to differences in the magnitude and

[3] The moisture flux includes water in vapor, liquid, and ice phases. Since only fluxes through the western and southern boundaries are considered, the drying ratio does not account for the flux of moisture into the domain from low-level easterly flow, which occurs during WRS storms (Figs. 3a–c). However, the moisture flux associated with such low-level easterly flow is very modest, amounting to no more than 4% of the flux through the western and southern boundaries in each storm. This is likely because the low-level easterly flow tends to be dry and shallow (see section 4 for further evidence of this). As a result, over the eastern boundary as a whole, the moisture flux is westerly at all times during all storms, explaining our decision to calculate the drying ratio based only on the moisture fluxes at the western and southern boundaries.

TABLE 2. Terms in the moisture budget of each storm that help us evaluate the theories that eastern precipitation during WRS storms is caused either by a reversal of the climatological rain shadow or by diminished orographic influence altogether. (second column) The westward flux of water vapor over the Cascade crest. (third column) The westward flux of condensed water (liquid + ice) over the Cascade crest. (fourth column) Net condensation over eastern slopes, with negative values indicating net evaporation. (fifth column) Precipitation over eastern slopes. (sixth column) The average drying ratio. Values in columns 2–5 have units of kg $\times 10^{11}$ h^{-1}. All values were calculated as the average over each storm's 6-h period of maximum precipitation.

	q_v flux	q_r flux	C_{east}	P_{east}	Drying ratio
WRS storms					
W1	2.10	0.68	0.74	1.07	0.56
W2	3.21	0.66	0.20	0.60	0.27
W3	3.20	1.09	0.51	0.98	0.42
SRS storms					
S1	8.27	1.49	−0.28	0.78	0.23
S2	6.61	1.33	−0.17	0.65	0.23
S3	8.33	1.29	−0.44	0.78	0.20

depth of descent. Indeed, this is precisely what we find in Fig. 6, where colors indicate the vertical wind speed w at hour 4 of each storm along a 150-km vertical cross section through the central Cascades (blue line in Fig. 1b). Over the western slopes (left side of each figure), the behavior of w is similar between WRS storms and SRS storms, with regions of alternating ascent (red shading) and descent (blue shading) bearing the signature of significant mountain-wave activity modulated by subrange-scale ridges and valleys. This is consistent with our earlier observation that orographic influence on west-slope condensation is similar across WRS and SRS storms, as indicated by roughly equal ratios of evaporation (from descent) to condensation (from ascent). Over eastern slopes, however, the similarities between WRS and SRS storms disappear. While SRS storms exhibit vigorous mountain waves—marked in particular by strong descent just east of the crest—wave activity is far less pronounced in each of the WRS storms, likely explaining why evaporation east of the crest is so much weaker in WRS storms than in SRS storms.

What might account for the difference in leeside mountain-wave amplitude between WRS and SRS storms? Previous studies suggest that low-level winds and static stability in the lee may play a role. For example, in idealized simulations of downslope wind storms, Lee et al. (1989) found that the presence of a stable cold-air pool in the lee of a mountain causes a significant reduction in mountain-wave amplitude and, thus, leeside descent, particularly when the cold air is held in place by an upslope geostrophic wind. Even more relevant to our present analysis, Zängl (2005) and Zängl and Hornsteiner (2007) found that, by suppressing descent, a leeside cold-air pool allows more precipitation to reach the lee slope, consistent with the relationship between leeside descent, evaporation, and precipitation we observe in the Cascades.

Might the suppression of leeside descent during WRS storms be caused by a layer of stable, stagnant air in the lee of the Cascades, as these previous studies suggest? To answer this question, vertical cross sections of horizontal wind speed are shown alongside vertical velocity in Fig. 6, with the contour of stagnant zonal winds ($U = 0$, thick black line). In addition, Fig. 7 shows the static stability at the same hour and cross section (colored contours), along with the $U = 0$ contour (black line), above (below) which the zonal wind is westerly (easterly). Comparing the location of the $U = 0$ contour in the WRS storms (left column) and SRS storms (right column), we find that during WRS storms, zonal winds are stagnant or easterly throughout the lower 1 or 2 km in the lee. During SRS storms, on the other hand, winds are generally westerly except in the deepest leeside valley (the Wenatchee), and then only below 700 m or so.

Turning our attention to the static stability in WRS storms (Fig. 7, colored contours), we find that regions where zonal winds are weak or easterly (primarily in the lee) also tend to be very stable, with a Brunt–Väisälä frequency approaching 0.02 s^{-1}—roughly equivalent to an isothermic cold-air pool. In contrast, during SRS storms, static stability is more spatially uniform, with no consistent change from east to west across the transect.

Together, the cross sections of zonal wind and static stability presented in Fig. 7 provide strong support for the hypothesis that the presence of a highly stable, stagnant-to-easterly cold pool is responsible for the suppression of leeside descent and evaporation during WRS storms and, thus, for the weak rain shadow itself. In the following sections, we examine this connection more closely through idealized simulations, focusing first on the relative importance of static stability and zonal wind speed, and then on the origin and evolution of cold-air pools during warm-frontal passage.

3. Influence of static stability and leeside winds

In this section we use idealized, two-dimensional numerical simulations to evaluate how rain-shadow strength depends on low-level stability and zonal winds in the lee of a mountain. Our simulations were performed using an updated version of the nonlinear, nonhydrostatic mesoscale model of Durran and Klemp (1983), configured exactly as described by Siler and Durran (2015) except for the treatment of surface friction, which we incorporate

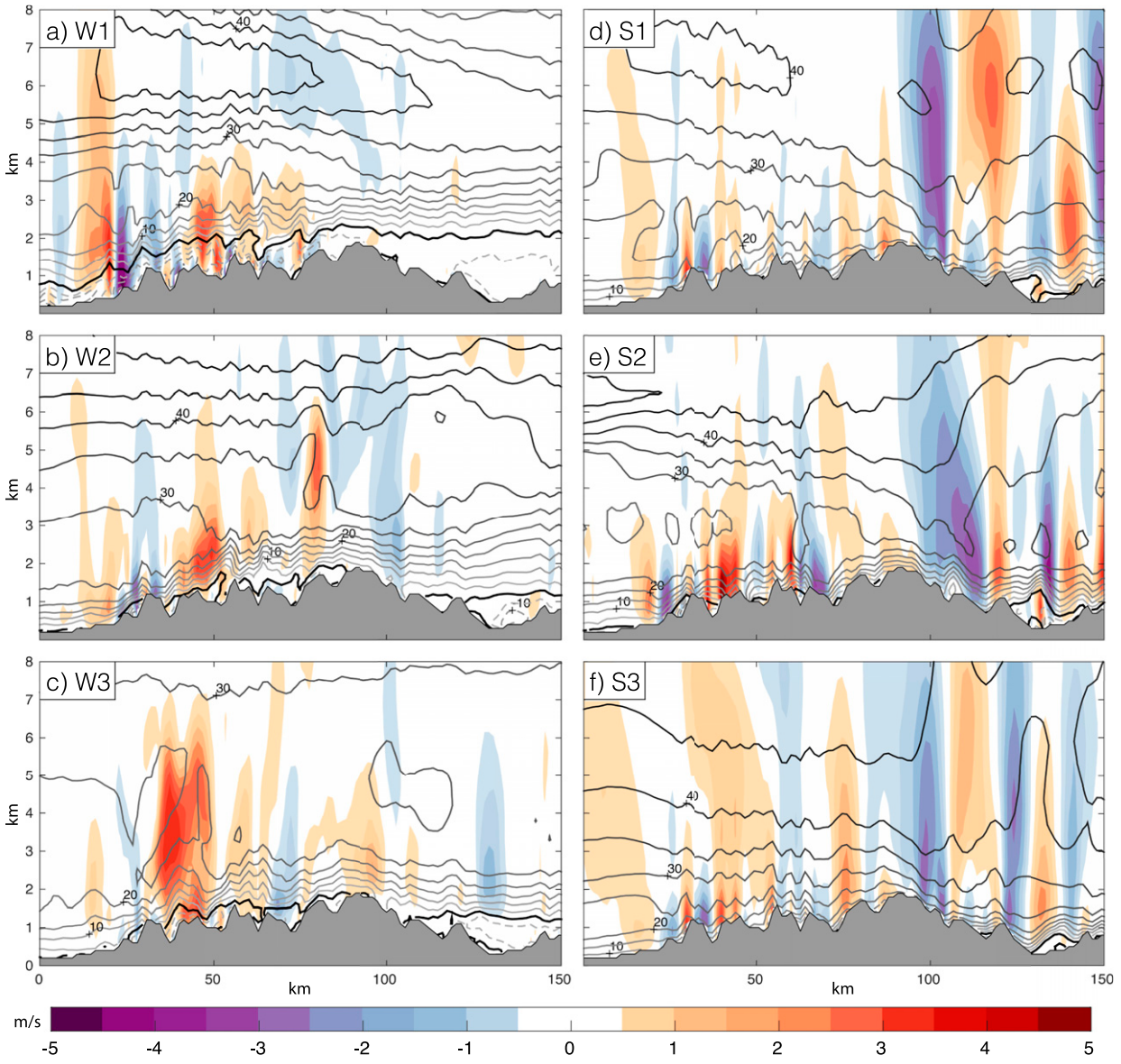

FIG. 6. Vertical velocity (colors; m s^{-1}) and the zonal component of the horizontal wind speed (gray contours; 5 m s^{-1} intervals) along the blue transect in Fig. 1, at hour 4 of each storm's 6-h period of maximum precipitation. The thick black contour represents $U = 0$, while dashed gray contours indicate $U < 0$. (left) WRS storms exhibit weaker descent immediately east of the crest, coincident with a deeper layer of easterly or stagnant zonal winds.

here using the boundary layer scheme of Zhang and Anthes (1982), as described in appendix B of Gaberšek and Durran (2006). Our domain consists of 800×150 x–z grid points, with a horizontal resolution of $\Delta x = 1$ km and a vertical resolution of $\Delta z = 100$ m. At the center of the domain is an idealized ridge with a profile given by

$$h(x) = \frac{h_0}{16}\left[1 + \cos\left(\frac{\pi x}{4a}\right)\right]^4, \qquad (1)$$

with maximum ridge height of $h_0 = 1.5$ km and a half-width of $a = 25$ km—similar to the dimensions of the Cascades. Upstream of the ridge, each simulation was initialized with a surface temperature of 280 K, a static stability of $N = 0.01$ s^{-1}, a relative humidity of 95%, and winds varying linearly between 12.5 m s^{-1} at the surface and 37.5 m s^{-1} at 10 km. Above 10 km the initial winds were constant with height. These conditions were chosen as a rough approximation of the case studies presented in the previous section. To eliminate spurious motion associated with a cold start, the wind speed was gradually increased to its stated value over the first two hours of each simulation.

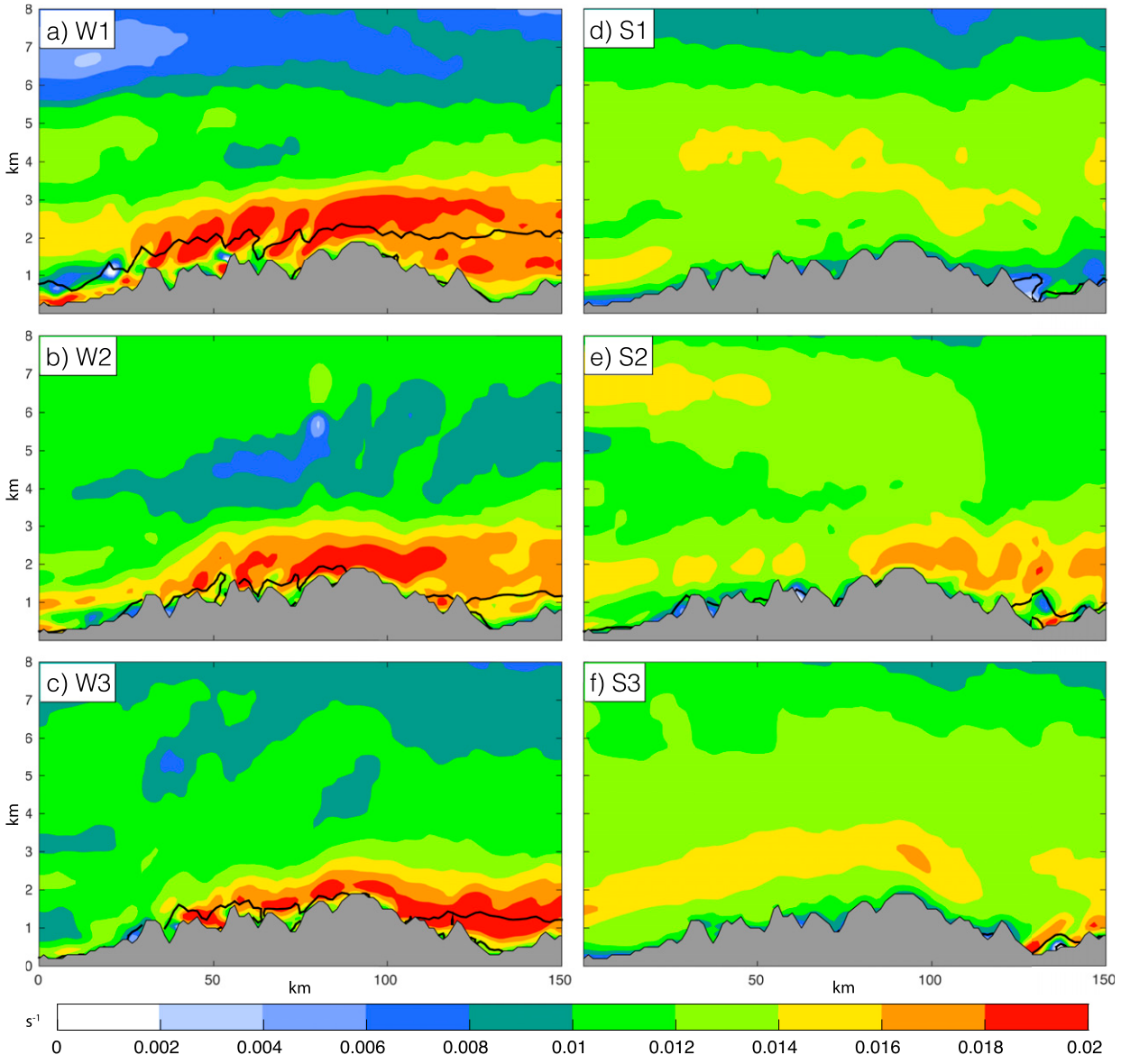

FIG. 7. Brunt–Väisälä frequency (s^{-1}) along the blue transect in Fig. 1, at hour 4 of each storm's 6-h period of maximum precipitation. The bold black contour represents $U = 0$, above (below) which the zonal wind is westerly (easterly).

To test the relative importance of static stability and zonal wind speed in modulating leeside descent and rain-shadow strength, we have performed four simulations, each initialized with the same conditions upstream of the crest, but with different conditions below crest level (i.e., below 1.5 km) in the lee.

In the first (control) simulation, U and N were initialized everywhere to their upstream values of $N = 0.01\,s^{-1}$ and $U = 12.5\ (37.5)\,m\,s^{-1}$ at the surface (10 km), roughly approximating the conditions present during SRS storms. In the second simulation ("stagnant lee"), static stability remained $N = 0.01\,s^{-1}$ everywhere, but the wind speed below 1.5 km in the lee was initialized to $U = -5\,m\,s^{-1}$, emulating the modest low-level easterly flow common to WRS storms in the Cascades. In the third simulation ("stable lee"), the wind speed was set to the control value, but static stability was increased to $N = 0.02\,s^{-1}$ below 1.5 km in the lee, representing an approximately isothermal cold pool. The final simulation ("stagnant + stable lee") incorporated both high stability ($N = 0.02\,s^{-1}$) and weak easterly flow ($U = -5\,m\,s^{-1}$) below 1.5 km in the lee and, therefore, represents the closest approximation of the actual conditions typically present during WRS storms.

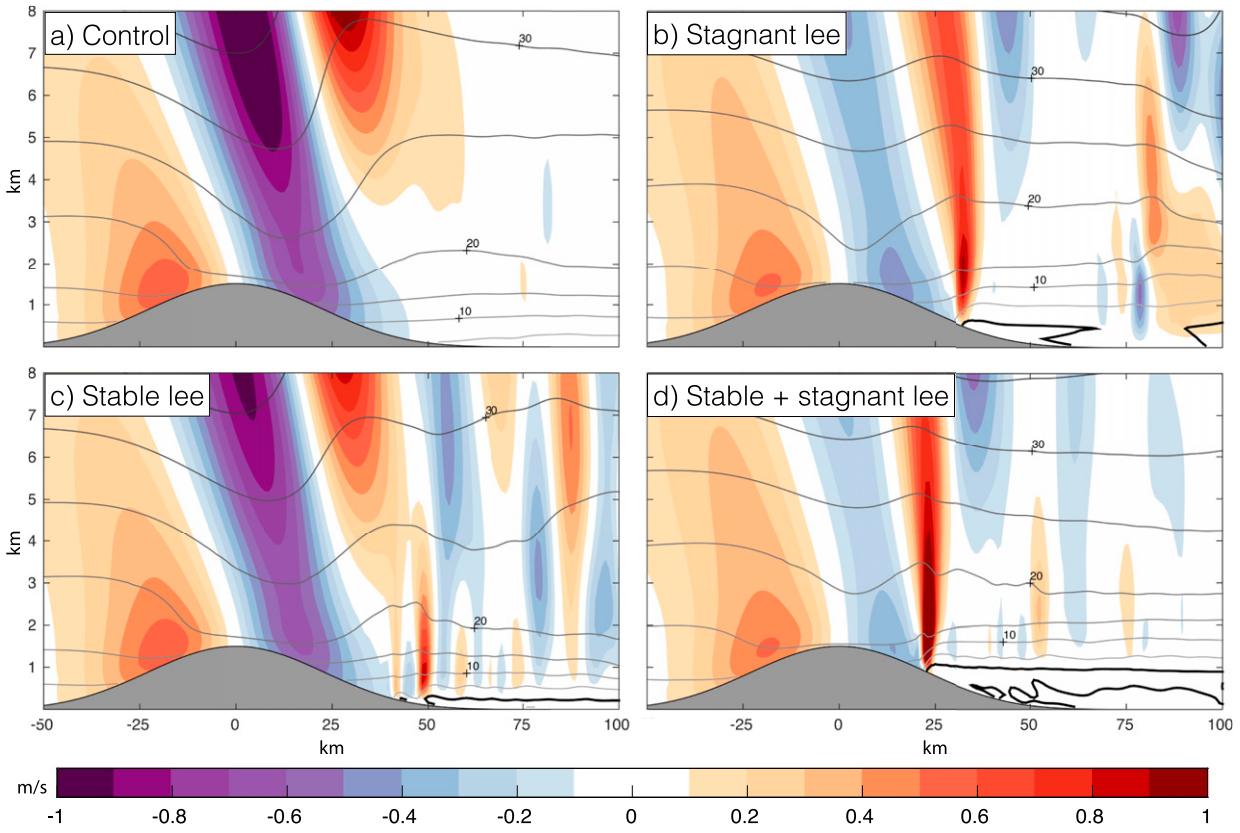

FIG. 8. Vertical velocity (m s^{-1}) and horizontal wind speed (gray contours; 5 m s^{-1} intervals) at hour 3 of each simulation. The thick black line represents $U = 0$. (a) Control, (b) $U = -5\,\mathrm{m\,s^{-1}}$, (c) $N = 0.002\,\mathrm{s^{-1}}$, and (d) $N = 0.002\,\mathrm{s^{-1}}$ and $U = -5\,\mathrm{m\,s^{-1}}$.

Figure 8 shows the vertical velocity (colors) and horizontal wind speed (gray contours) at hour 3 of each simulation. In the control simulation (Fig. 8a), we find the classic mountain-wave pattern, with a region of vigorous descent in the lee tilting upstream with height. Interestingly, similar behavior is found in the high-stability simulation (Fig. 8c), with leeside descent only slightly weaker than in the control case. This demonstrates that a stable layer that moves with the background flow has minimal impact on leeside descent.

In contrast, the two cases with stagnant air at low levels in the lee exhibit much weaker leeside descent than the control simulation (Figs. 8b,d). The reason is obvious from the horizontal wind field, which shows that descent along the lee slope stops abruptly where $U \leq 0$ (i.e., where winds are stagnant or easterly). Over the course of each simulation, the stagnant layer is gradually eroded by the overlying flow, and the $U = 0$ line moves progressively down the lee slope, with descent strengthening in the process. Comparing Figs. 8b and 8d, it is clear that a stronger stability makes the stagnant layer more resilient to erosion, and this has important implications for the persistence of weakened descent, as we discuss below. At a particular moment, however, the magnitude of leeside descent seems to be determined only by the depth of stagnant air in the lee.

Differences in leeside descent have a strong impact on cloud water and precipitation downstream of the crest, as evident in Fig. 9 and Fig. 10. In the cases with strong descent (Figs. 9a,c), very little cloud water persists beyond 25 km downstream of the crest, and precipitation is similarly absent from the far lee (Fig. 10, black and green lines). On the other hand, in cases with weaker leeside descent, clouds and precipitation extend much farther downstream, owing in part to a lower rate of evaporation in descending regions, but also to strong updrafts at the leading edge of the stagnant layer (Figs. 8b,d), which cause a significant jump in cloud water and precipitation locally. As a result, the ratio of west-slope precipitation to east-slope precipitation—the same measure of rain-shadow strength used in Table 1—varies significantly across the simulations, ranging from 2.2 when descent is strong (Figs. 8a,c) to around 1 when descent is suppressed by stagnant air in the lee (Figs. 8b,d).

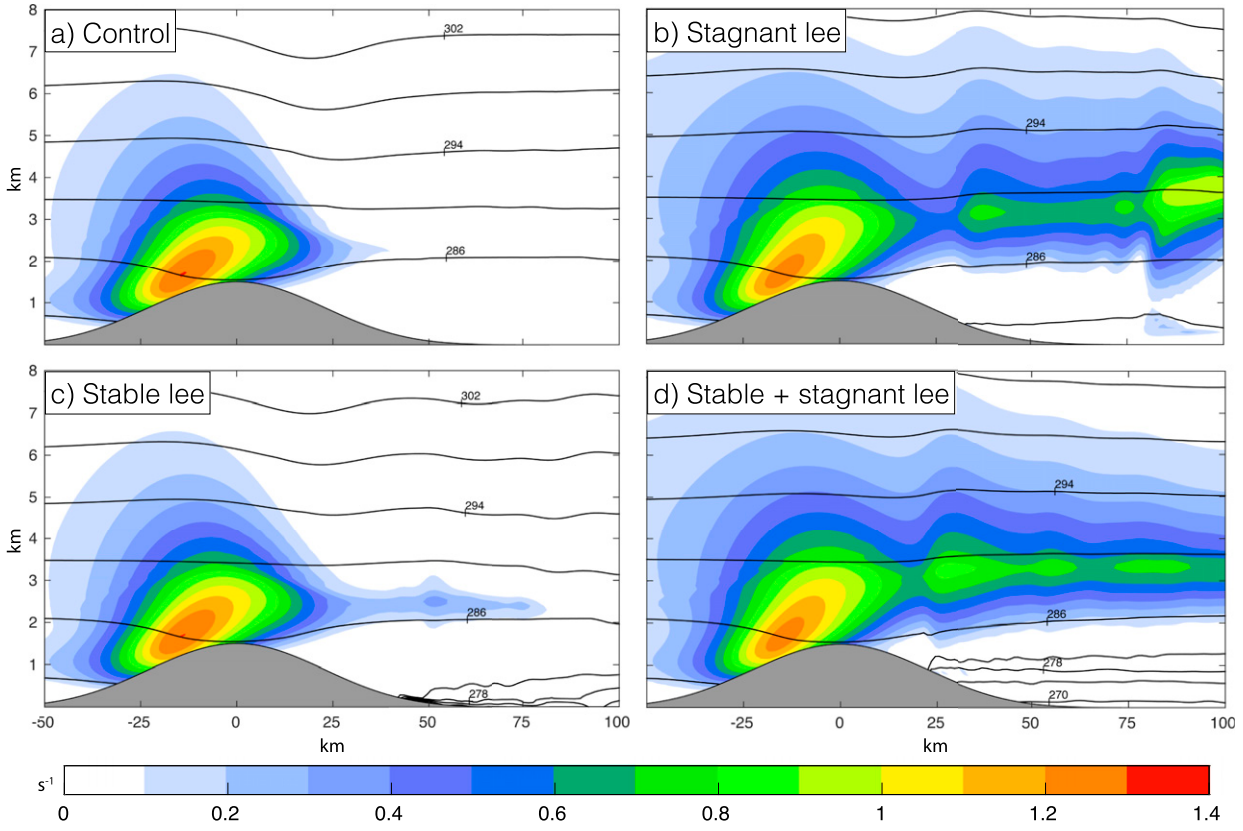

FIG. 9. Total liquid water mixing ratio (colors; g kg^{-1}) and potential temperature (black contours) at hour 3 of each simulation. (c),(d) The larger vertical gradients in potential temperature indicate higher static stability. (a) Control, (b) $U = -5\,\mathrm{m\,s^{-1}}$, (c) $N = 0.002\,\mathrm{s^{-1}}$, and (d) $N = 0.002\,\mathrm{s^{-1}}$ and $U = -5\,\mathrm{m\,s^{-1}}$.

As noted above, however, stagnant air in the lee does not persist indefinitely but is gradually eroded over time. Figure 11 shows the impact of this erosion on the strength of the rain shadow, as measured by the ratio of western to eastern precipitation. When the stability of the stagnant layer is the same as the background flow (blue line), the rain shadow starts off weak but increases rapidly, approaching its equilibrium value of around 1.65 by hour 4 of the simulation. On the other hand, when the stagnant layer is more stable than the background flow (red line), the rain shadow strengthens much less (to 1.25 by hour 10), suggesting that a stable layer of stagnant air is more resilient to erosion—and thus more persistent—than a stagnant layer with lower stability.[4]

These results suggest that stability and wind speed both play a crucial role in the suppression of leeside descent during WRS storms. By itself, a layer of high stability east of the crest will not suppress leeside descent without sufficient inertia to remain in place. Conversely, while stagnant or easterly flow in the lee may suppress descent for a short time, it will quickly be eroded without the stability to push back against air plunging over the crest. When combined, however, high stability and stagnant-to-easterly zonal winds at low levels east of the crest can sharply constrain leeside descent and evaporation over a period of several hours, likely contributing to the weak gradients in leeside precipitation that are the defining characteristic of WRS storms.

4. Evolution of semi-idealized event

a. *Experiment description*

While the 2D simulations demonstrate how a stagnant, stable layer in the lee can weaken the rain shadow, they provide no insight into the development and evolution of these layers in nature. To shed light on this

[4] The cases without a stagnant layer in the lee also show some evolution in rain-shadow strength, presumably resulting from drift in the upstream conditions. However, the magnitude of the change is modest, decreasing from 2.2 at hour 3 to 1.8 by hour 10—similar to the equilibrium value reached after the stagnant air is eroded in Fig. 11.

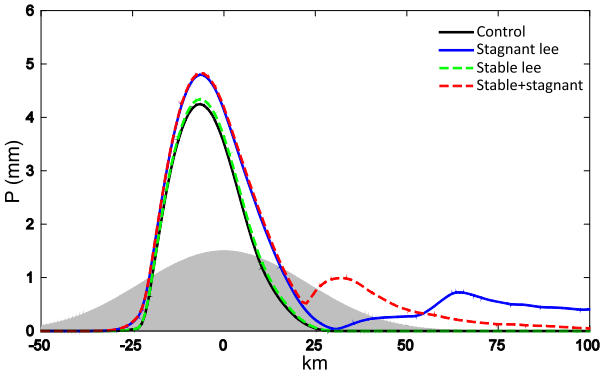

FIG. 10. Precipitation (mm) between hours 2.5 and 3.5 of each simulation, as a function of distance across an idealized 2D ridge (shaded gray). Control (black), $U = -5\,\mathrm{m\,s^{-1}}$ (blue), $N = 0.002\,\mathrm{s^{-1}}$ (green), and $N = 0.002\,\mathrm{s^{-1}}$ and $U = -5\,\mathrm{m\,s^{-1}}$ (red).

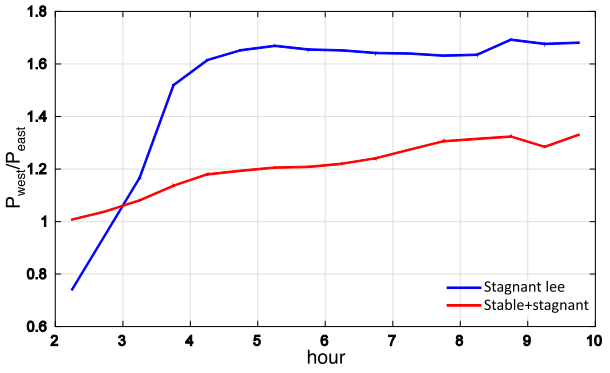

FIG. 11. Ratio of precipitation east and west of the crest as a function of simulation hour, for the simulations initialized with $U = -5\,\mathrm{m\,s^{-1}}$ and $N = 0.01\,\mathrm{s^{-1}}$ (blue) or $N = 0.02\,\mathrm{s^{-1}}$ (red).

question, here we present results from a WRF simulation involving a real WRS storm, but with the Cascades replaced by an idealized, quasi-2D ridge, intended to fully account for 3D effects and to separate the effects of meridional variations in synoptic storm structure from meridional variations in the shape of the terrain. We have chosen to focus on the third WRS storm (W3) discussed in section 2 above, primarily because, of the three WRS storms, it produced the most precipitation. The model was configured exactly as in the earlier simulations presented in section 2, but with modified topography consisting of an idealized ridge with a maximum height of 2 km and a half-width of 0.5° longitude, which straddles the −121.25° meridian between 45.5° and 50° latitude. West of the crest, the shape of the ridge is defined by Eq. (1). However, this equation was adjusted east of the crest to give a minimum elevation of 500 m, as a rough approximation of the Columbia Plateau. To the north and south of the ridge, a transition to realistic topography was implemented over a distance of 2° of latitude using bilinear interpolation. To the east, the transition was implemented over 2.5° of longitude, beginning at −119° longitude. The same topographic modification was incorporated in all four nested grids but is shown for only the innermost grid in Fig. 12, which can be compared directly to the real topography in Fig. 1b.

Figures 13–17 track the evolution of the storm at 2-h intervals over a 10-h period from 1800 UTC 14 December to 0400 UTC 15 December 2006. The top row of each figure shows the total precipitation and column-integrated condensation occurring over the 2-h period beginning an hour before the stated time, as well as the instantaneous horizontal winds at 1.5 and 3 km and the potential temperature at 1.5 km. The next two rows show vertical cross sections of the (instantaneous) vertical and zonal wind speeds (left) and potential temperature and condensed water (right) along two different transects: one at 48.5° latitude (top) and the other farther south at 47° latitude (bottom).

b. Results

At hour 1 of the storm (Fig. 13), precipitation has begun to fall in the southern half of the domain. Along the southern transect, winds over the western slope are westerly above 500 m, resulting in significant ascent (Fig. 13f). However, because of weak zonal winds at the surface, ascent is strongest above 5 km where there is less moisture, and therefore, rates of condensation (Fig. 13b) and precipitation (Fig. 13a) are relatively modest. Over the eastern slope, descent is inhibited by zonally stagnant winds below crest level, much like in the 2D simulations discussed in the previous section. In addition, the close spacing of the isentropes just east of the crest (Fig. 13g, black lines) indicates high stability, again consistent with earlier simulations. The high stability is due to cold air at low levels east of the crest (Fig. 13c), which remains in place even as the front brings warmer air above and west of the crest. In the north, winds are easterly at low levels, with very strong veering through the lower 3 km (Fig. 13c), indicative of strong warm-air advection. While this brings a reversal of the climatological rain shadow directly over the Cascades (Fig. 13a), the shallowness of the easterly layer precludes significant orographic enhancement (Figs. 13d,e), resulting in very light precipitation over the eastern slope.[5]

[5] This scenario appears to be similar to the reverse-rain-shadow example discussed by Mass et al. (2015, their Fig. 9), which likewise exhibits very light precipitation over the eastern slope (~0.1 inch in a 3-h period). This is consistent with our assessment in section 2 that easterly upslope flow has little direct impact on a storm's overall precipitation pattern.

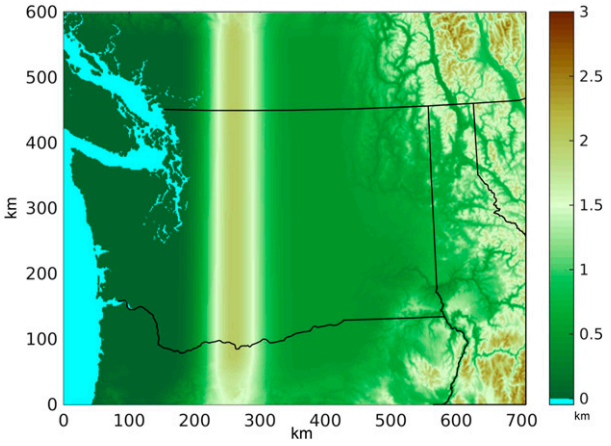

FIG. 12. The innermost grid in which the Cascades have been replaced by an idealized ridge, with colors representing terrain elevation (km).

By hour 3, precipitation is falling over much of the region, but the nature of the precipitation differs significantly from north to south. Along the southern transect, precipitation over the western slope is primarily generated by strong upslope flow (Fig. 14f). East of the crest along this transect, descent has begun to develop near the crest, but it is very weak, inhibited by a stable, zonally stagnant layer that extends from the surface almost to the crest. The absence of strong leeside descent allows precipitation generated by large-scale ascent and spillover to reach the surface without evaporating (Fig. 14a).

Meanwhile, along the northern transect, conditions resemble those in the south 2 h earlier. Over the lower western slope, the $U = 0$ line (Fig. 14d, thick black line) has descended several hundred meters from its earlier position (Fig. 13d), but easterly flow persists in the lowest 500 m. The sloping structure of the $U = 0$ line, along with the isentropes (Fig. 14e), suggests the presence of a warm front, which roughly parallels the western slope just above the surface. This interpretation is further supported by the presence of large-scale ascent (Fig. 14d) and by the relatively uniform distributions of precipitation and condensation across the transect (Figs. 14a,b).

Five hours into the storm, the cold, zonally stagnant layer has finally been eroded to a depth of less than 1 km in the south, allowing a descending wave to set up over the lee slope (Fig. 15f). The evaporation caused by this descent eliminates most of the cloud water (Fig. 15g) and precipitation (Fig. 15a) east of the crest, resulting in a strong rain shadow.

In the north, conditions east of the crest have changed little since the previous period, with widespread ascent and condensation resulting from large-scale ascent (Figs. 15b,d). West of the crest, however, westerly winds now extend down to the surface, causing strong orographic ascent and condensation over the western slope (Fig. 15d). Much of the resulting condensate is carried over the crest and becomes precipitation on the eastern slope, aided by the absence of downdrafts that might otherwise cause it to evaporate before reaching the surface. The east-slope precipitation is heavy and exceeds the east-slope condensation by a factor of 2. In fact, east-slope precipitation exceeds west-slope precipitation along the northern transect by 26%, even though condensation is three times greater west of the crest.

By hour 7 of the storm, the zonally stagnant layer in the south has largely been eroded away, allowing very strong descent to form along the lee slope (Fig. 16f), accompanied by the intrusion of potentially warm air from the west (Fig. 16c). As a result, precipitation along the lee slope is confined close to the crest (Figs. 16a). To the north, large-scale condensation has weakened significantly over the lee slope (Fig. 16b), but a layer of stable, zonally stagnant air fills the entire basin from the surface to the crest (Fig. 16d), preventing any leeside descent and evaporation. Combined with a reduction in windward precipitation, the end result is an even weaker rain shadow than before, with east-slope precipitation exceeding west-slope precipitation by 73% along the transect.

Finally, 9 h after the storm began to impact the region, the front has passed through, and precipitation is confined primarily to the western slope of the ridge in both the north and south, with streaks bearing evidence of postfrontal convective showers (Fig. 17a). While most of the precipitation from the storm has passed, it is nevertheless noteworthy that the leeside stagnant layer remains in place in the north, preventing any significant descent from occurring over the lee slope, and thus allowing clouds and drizzle to persist well into the lee (Figs. 17d,e). The high stability of this layer ($N \approx 0.02\,\mathrm{s}^{-1}$) very likely contributes to its persistence, as demonstrated in the 2D simulations discussed previously.

To gain a more quantitative understanding of the storm's progression, we present in Table 3 the net condensation and precipitation integrated along the eastern and western slope of each transect during the same 2-h periods corresponding to Figs. 13–17. Throughout the storm, condensation exceeds precipitation along the western slope of both transects, indicative of spillover to the eastern slope. East of the crest, however, the early stages of the storm (e.g., hours 1 and 3) are characterized by roughly equal amounts of condensation and precipitation, implying that east-slope precipitation during this period comes primarily from local condensation rather than spillover. Based on our analysis above, such

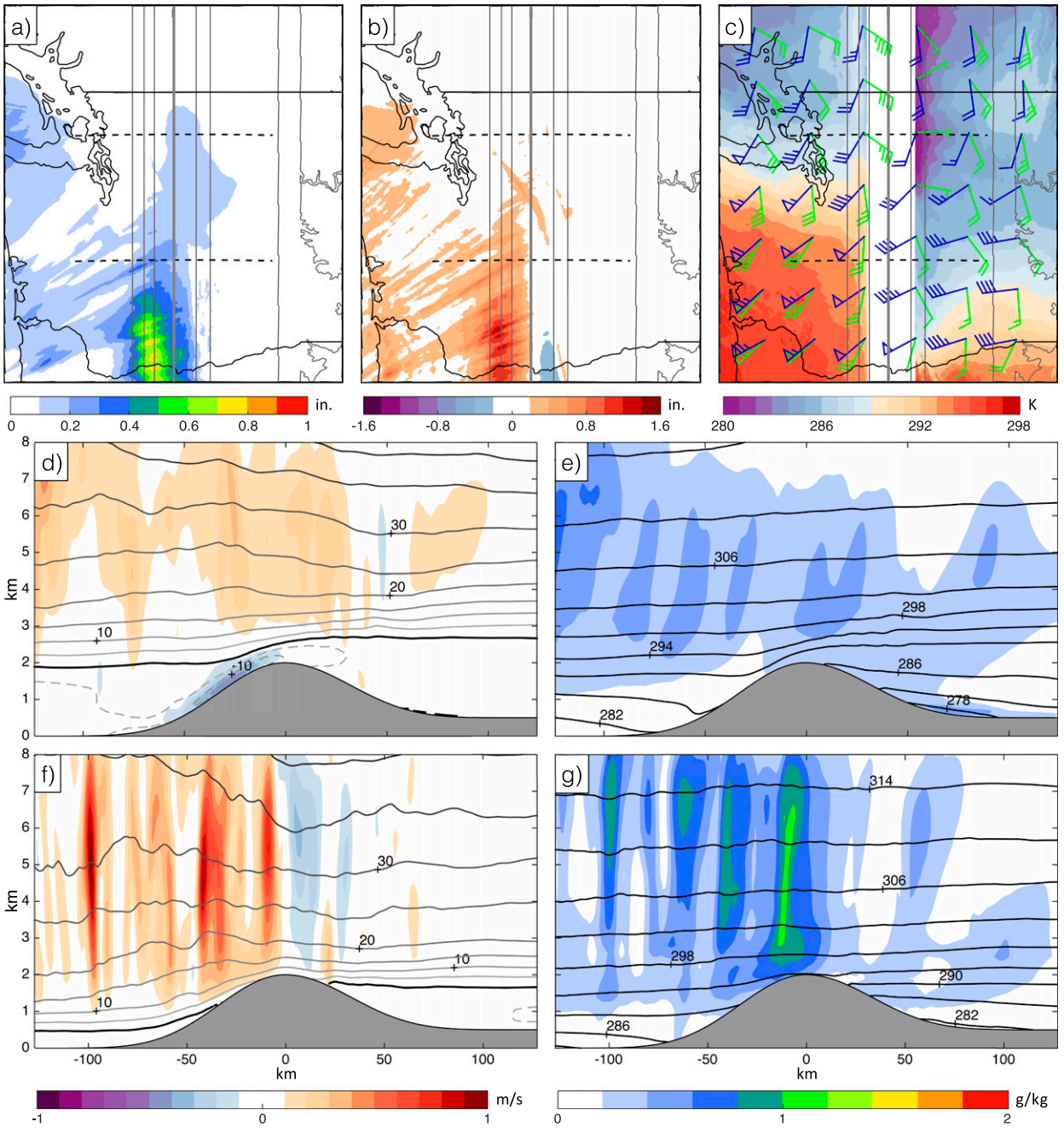

FIG. 13. Conditions at hour 1 of the storm. (a) Two-hour precipitation (in.) between hours 0 and 2 of the storm. Terrain elevation is shown in gray, contoured at 500-m intervals. The thick gray line represents the crest. (b) Two-hour column-integrated condensation (in.) over the same period. (c) Instantaneous potential temperature at 1.5 km (colors), and horizontal wind barbs (kt) at 1.5 (green) and 3 km (blue). (d) Vertical velocity (colors; m s^{-1}) and zonal wind speed (gray contours; 5 m s^{-1} intervals) along the northern transect (dashed line) shown in (a)–(c). The bold black line represents $U = 0$. (e) Total cloud plus hydrometeor mixing ratio (colors; g kg^{-1}) and potential temperature (black contours) along the northern transect. (f),(g) As in (d),(e), but for the southern transect.

east-slope condensation is mostly generated by large-scale ascent, though there is some evidence that easterly upslope flow contributes to modest orographic enhancement at hour 1 in the north (Figs. 13d,e). As the storm progresses (e.g., hours 5–9), condensation gives way to evaporation east of the crest in the south as the stagnant layer is gradually eroded, causing the rain shadow to strengthen. In the north, condensation gradually diminishes over time but never turns to evaporation owing to the persistence of the stagnant layer. This

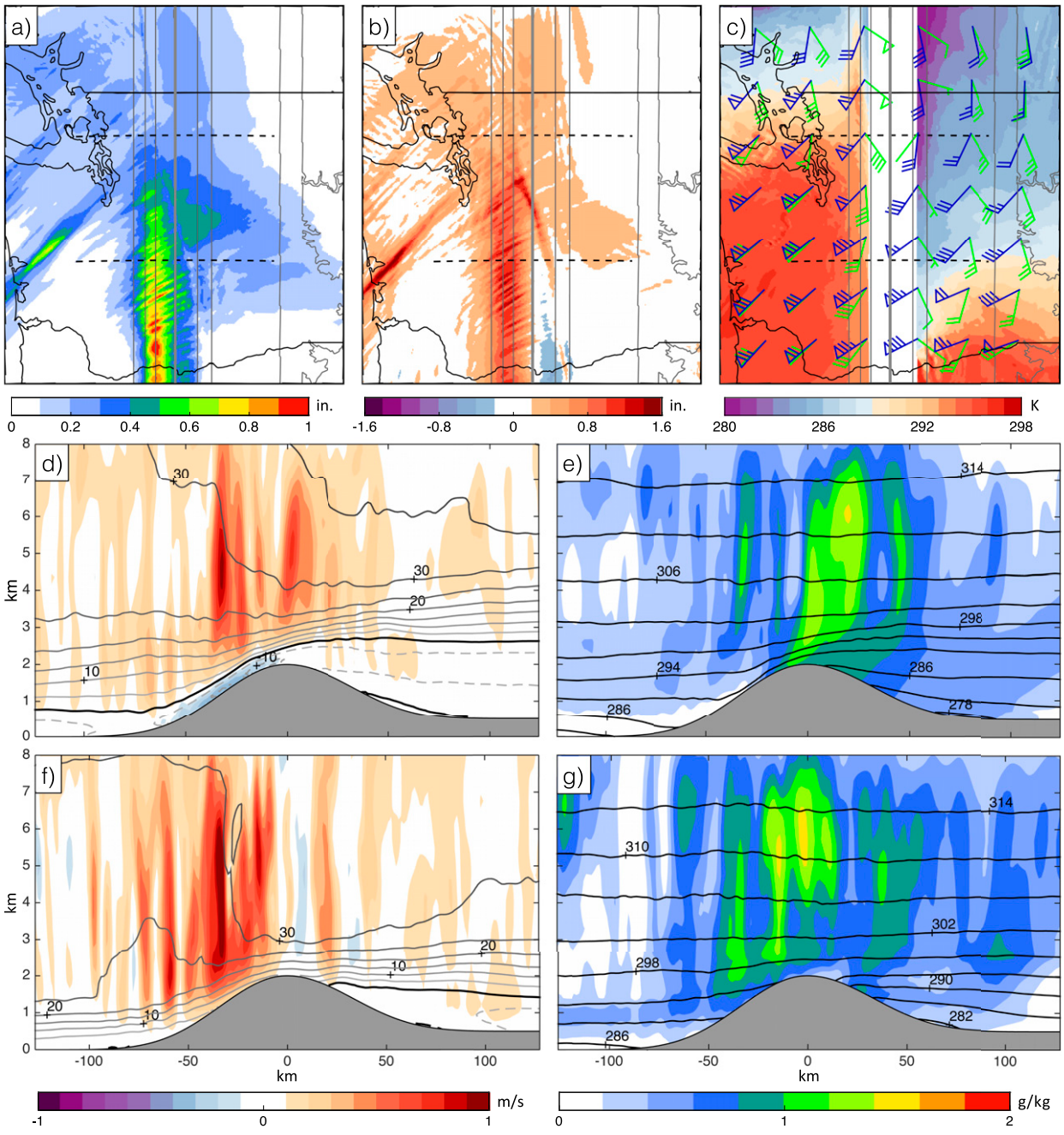

FIG. 14. As in Fig. 13, but at hour 3 of the storm.

permits large amounts of condensate to spill over the crest, resulting in even more precipitation on the eastern slope than on the western slope during hours 5 and 7.

5. Discussion

Together, Figs. 13–17 illustrate the progression of the rain shadow as a midlatitude cyclone impacts a mountain range. This process can roughly be divided into four stages, which are illustrated schematically in Fig. 18. First, before the surface warm front arrives, low-level winds are southerly to southeasterly everywhere, while large-scale ascent produces light precipitation (Fig. 18, top left). While there may be upslope flow east of the crest, it has little impact on precipitation because the easterly layer is shallow and relatively dry. In the second stage (Fig. 18, top right), the surface front crosses the ridge from the west, bringing strong upslope flow over

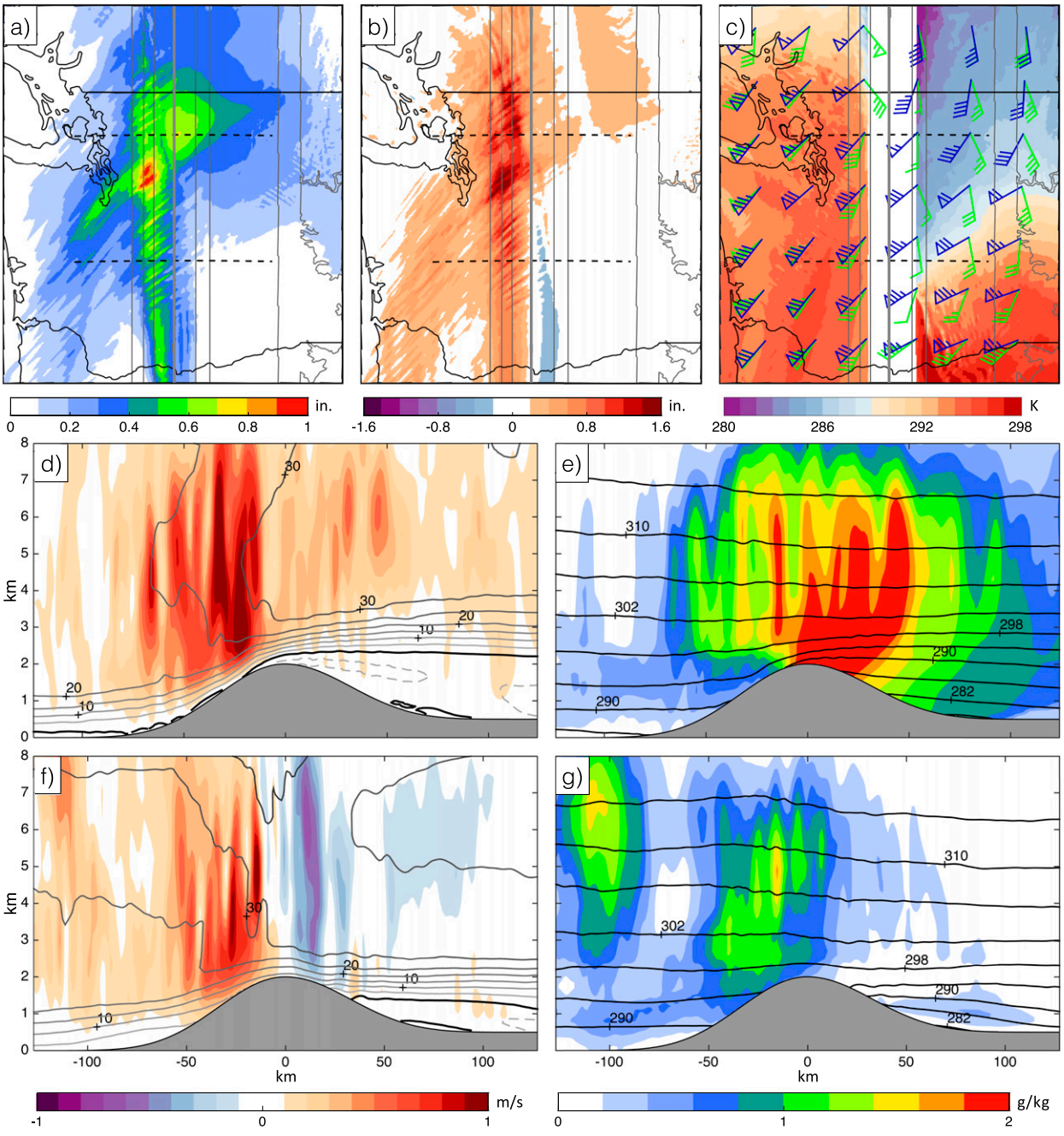

FIG. 15. As in Fig. 13, but at hour 5 of the storm.

the western slope, accompanied by significant orographic enhancement of condensation. East of the crest, the front is blocked by the ridge at low levels, allowing cold, zonally stagnant air to persist. Above the crest, the front continues to cause large-scale ascent, but its contribution to precipitation is modest compared to spillover precipitation from the western slope. In the third stage (Fig. 18, bottom left), the front has passed through at all levels, and the western slope continues to experience significant enhancement of condensation and precipitation from upslope flow within the storm's warm sector. However, in the wake of the front, cold, zonally stagnant air remains in place below crest level in the lee, buttressed by an increase in stability as the front brings warmer air aloft. As a result, leeside descent and evaporation are inhibited and the weak rain shadow persists. In the final stage (Fig. 18, bottom right), the stagnant layer is eroded and the flow turns westerly

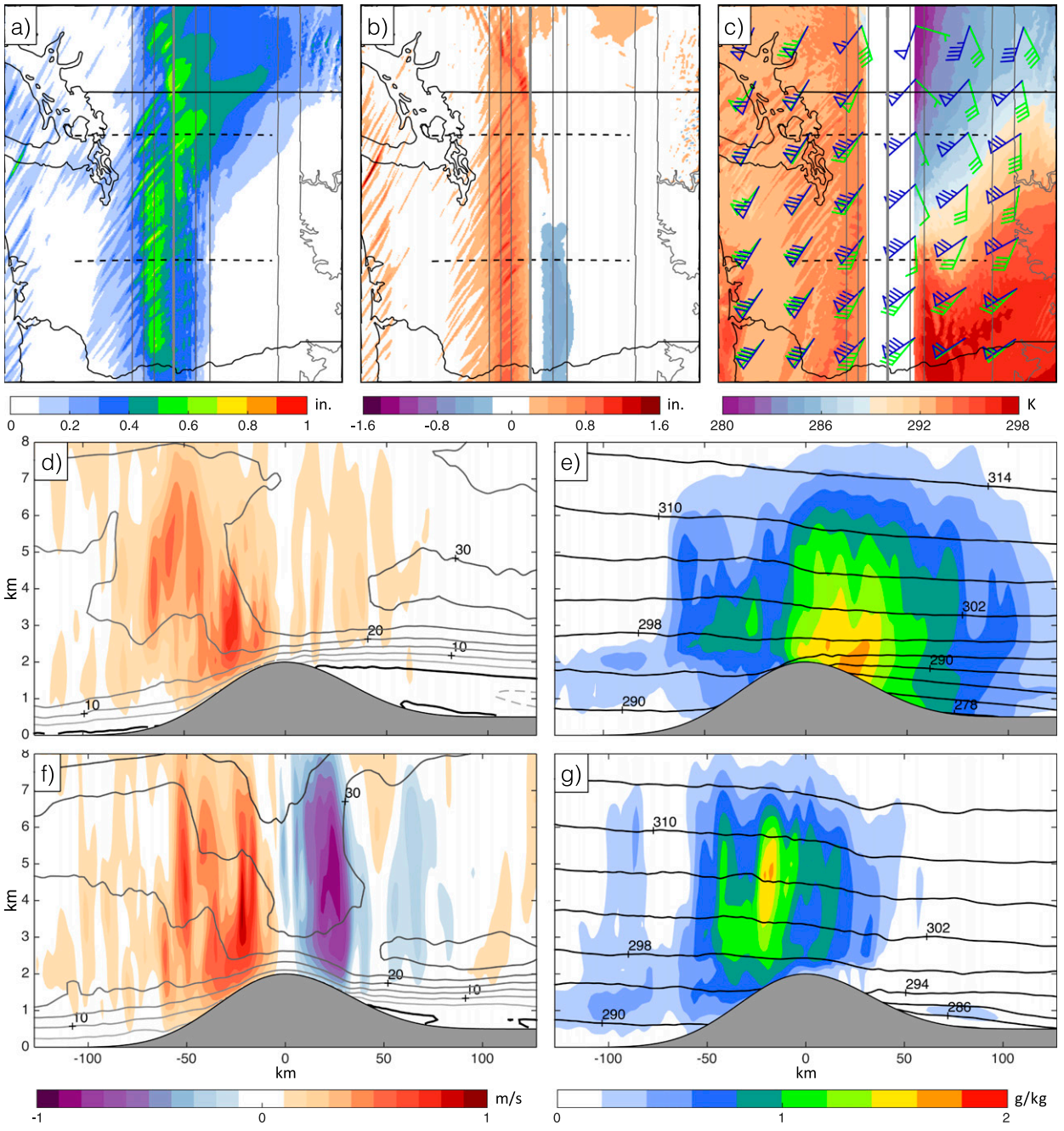

FIG. 16. As in Fig. 13, but at hour 7 of the storm.

everywhere, bringing vigorous descent east of the crest and a strong rain shadow. The transition between the third and final stages seems to depend largely on the stability of the stagnant layer, with higher stability making the layer more resistant to erosion by the overlying westerly flow.

For the storm as a whole, therefore, rain-shadow strength depends on the relative importance of each stage. In SRS storms, the first three stages either do not occur at all or pass rather quickly, with most of the precipitation occurring during the final stage, when there is no stagnant layer suppressing descent in the lee. This is consistent with the earlier observation by Siler et al. (2013) that precipitation from SRS storms occurs almost exclusively within the storm's warm sector and not during warm-frontal passage. During WRS storms, on the other hand, a larger fraction of precipitation occurs in the second and third stages, when the combination of

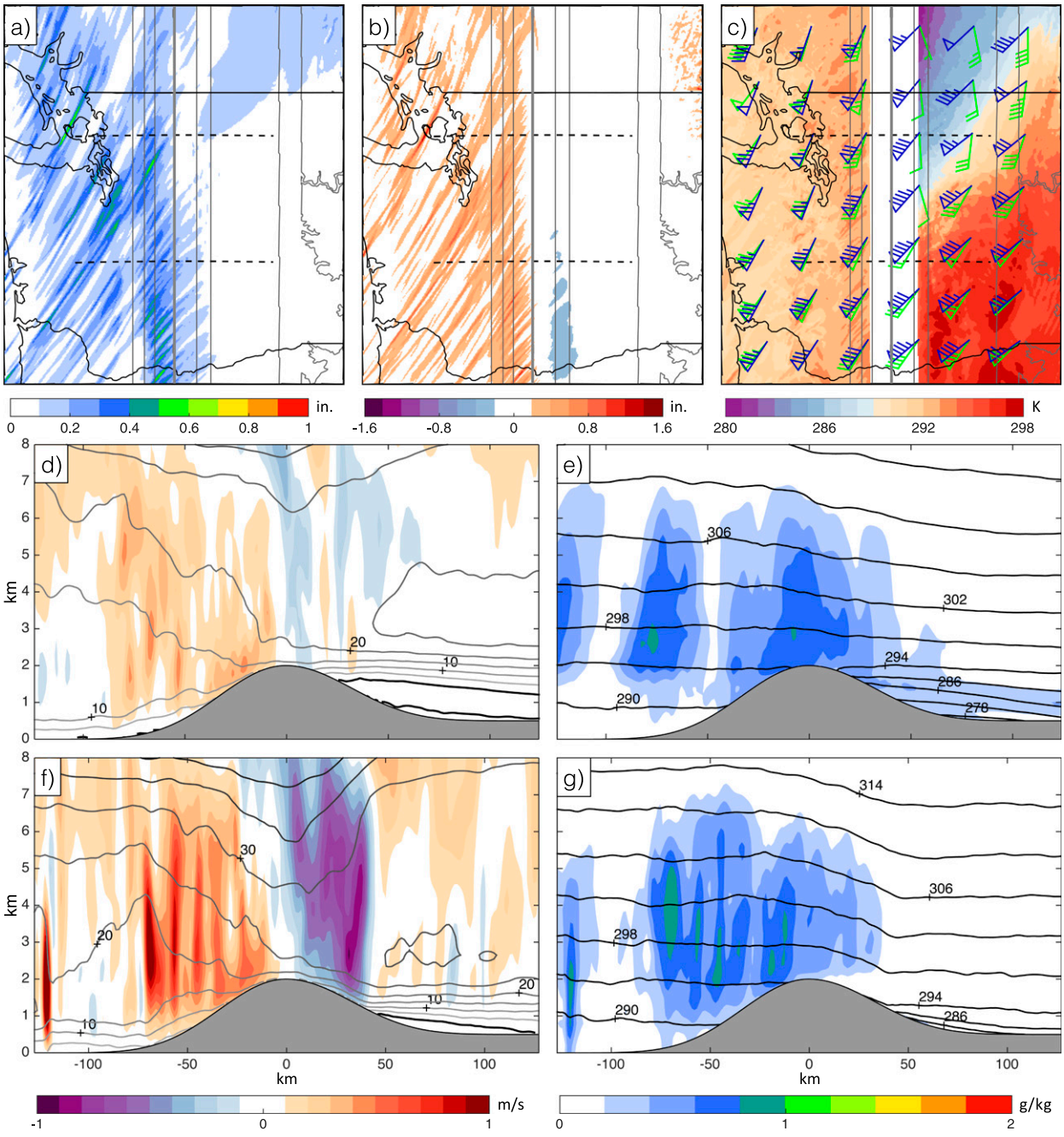

FIG. 17. As in Fig. 13, but at hour 9 of the storm.

western upslope flow and stagnant air in the lee allows for significant precipitation east of the crest, both from orographic spillover and large-scale ascent. A strong front will also add stability to the stagnant layer, which makes it more resilient to erosion. Thus, by the time a WRS storm progresses to the fourth stage, precipitation may have largely passed, resulting in a weak rain shadow for the storm overall.

These differences between WRS and SRS storms are consistent with another key finding of Siler et al. (2013)—namely, that on climate time scales, the strength of the Cascade rain shadow is controlled by storm-track latitude. Evidence of latitude dependence is clear in Fig. 19, which shows the pattern of precipitation (left) and column-integrated condensation (right) over the 10-h period discussed above. While the

TABLE 3. Net condensation and precipitation, integrated along portions of each transect during each 2-h interval of the storm ($kg \times 10^3\ m^{-1}$). (second column) Integrated net condensation over the western slope. (third column) Integrated precipitation over the western slope. (fourth column) Integrated net condensation over the eastern slope, with negative values indicating net evaporation. (fifth column) Integrated precipitation over the eastern slope.

	C_{west}	P_{west}	C_{east}	P_{east}
North				
Hour 1	3.08	2.25	3.15	2.16
Hour 3	11.88	7.19	5.25	5.40
Hour 5	21.65	12.17	7.24	15.29
Hour 7	9.73	7.39	3.26	12.78
Hour 9	6.43	5.44	0.03	2.42
South				
Hour 1	10.37	5.33	1.66	2.41
Hour 3	17.61	10.57	6.62	7.82
Hour 5	16.99	11.92	−1.30	3.39
Hour 7	13.73	9.47	−4.50	4.52
Hour 9	9.36	6.75	−1.63	1.74

southern end of the domain is characterized by a strong rain shadow and net evaporation in the lee, the rain shadow becomes progressively weaker to the north as evaporation gives way to (weak) condensation over the eastern slope. Thus, while it is not surprising that this storm exhibited one of the weakest rain shadows of the 100 storms in our dataset, it would likely be classified as a SRS storm if we were focused on the Oregon Cascades, or if it were translated just a few degrees to the north.

6. Summary and conclusions

In this paper, we have investigated the dynamical differences between weak-rain-shadow (WRS) and strong-rain-shadow (SRS) storms in the Washington Cascades. Consistent with previous studies, we found that WRS storms exhibit more warm-air advection than SRS storms, with correspondingly greater veering of the winds with height. While strong veering can result in easterly upslope flow in the early stages of WRS storms, there is little evidence that this contributes to significant local orographic enhancement of precipitation over eastern slopes. Instead, in comparison to SRS storms, WRS storms are characterized by weaker descent and evaporation over the eastern slopes, allowing more condensed water to reach the surface, and resulting in a more equal distribution of precipitation between western and eastern slopes. Using idealized two-dimensional simulations, we found that weak leeside descent during

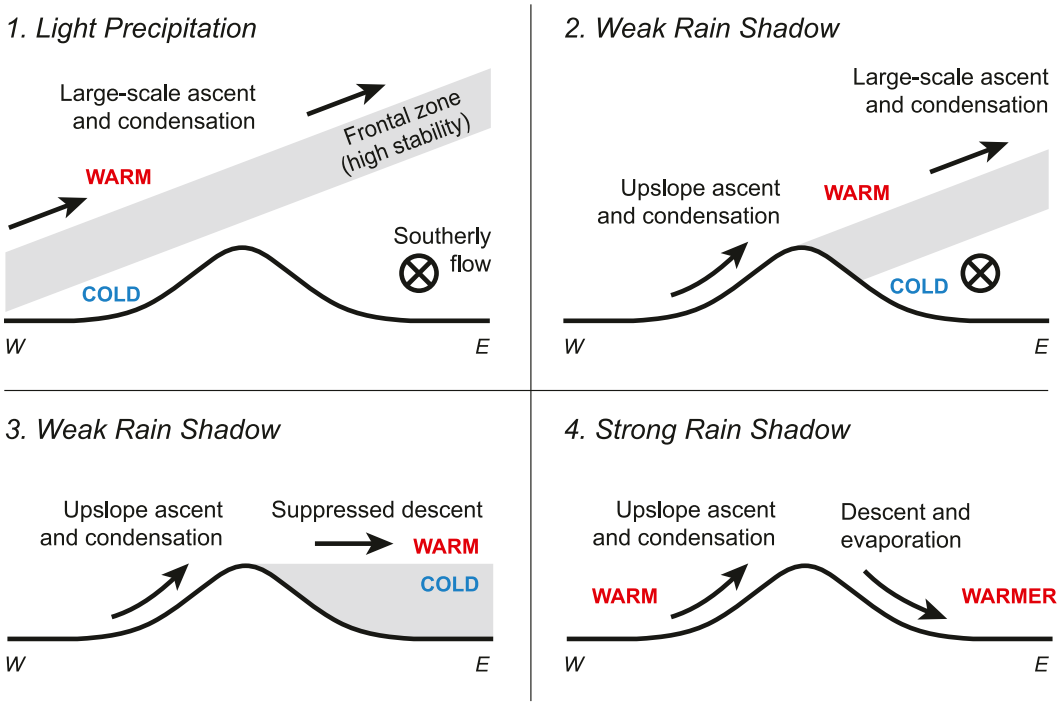

FIG. 18. Schematic illustration of the four stages of warm-frontal passage over a quasi-2D mountain range. Each figure represents a vertical cross section in the east–west plane. Gray shading represents the frontal zone, indicative of high stability and strong veering of the winds with height. Below the frontal zone, the flow is southerly and relatively cool. Above the frontal zone, the flow is westerly and relatively warm.

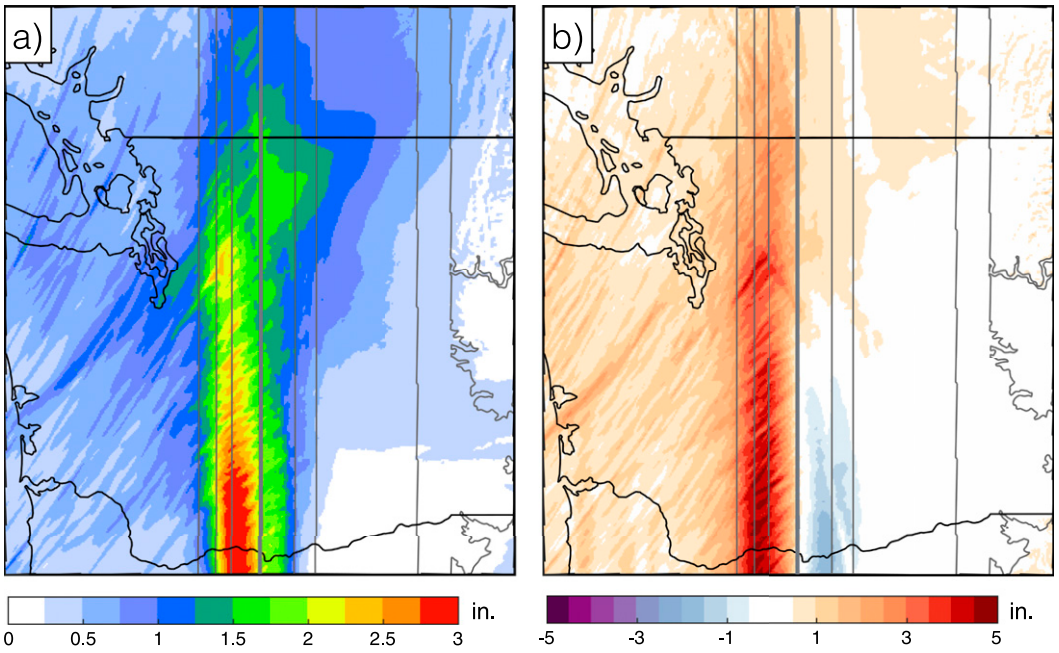

FIG. 19. Total (a) precipitation and (b) column-integrated condensation over the 10-h period discussed in Figs. 13–17. Terrain elevation is shown in gray, contoured at 500-m intervals. The thick gray line represents the crest.

WRS storms can be attributed to a persistent layer of stable, zonally stagnant air at low levels in the lee. In a numerical simulation of an historical WRS storm performed with an idealized ridge, we found that the leeside stagnant layer precedes the warm front and remains in place as the front is blocked by the ridge at low levels. Meanwhile, the intrusion of warm air aloft increases the stability of the zonally stagnant layer, making it more resistant to erosion by the overlying flow, and causing the weak rain shadow to persist long after the front has passed. This effect was clearly illustrated along the northern transect of our semi-idealized simulation, where east-slope precipitation exceeded west-slope precipitation by 10%, even though condensation was nearly three times greater over the western slope.

Based on this analysis, we have proposed a four-stage progression of warm-frontal passage over a mountain range, with a strong rain shadow emerging only in the fourth stage, after the zonally stagnant layer has been eroded away by the overlying westerly flow. Therefore, in places where there is minimal warm-air advection (e.g., in the storm's warm sector), progression to the fourth stage occurs quickly, resulting in a strong rain shadow for the storm overall. On the other hand, where the warm front is strong, the zonally stagnant layer might outlast the storm itself, resulting in an overall weak rain shadow. This explains the connection between warm fronts and weak rain shadows that previous studies have found.

In a broader context, our results suggest that, all else being equal, the rain shadow should weaken with latitude in mountain ranges where precipitation comes primarily from midlatitude cyclones. This effect has been demonstrated in idealized simulations with a general circulation model [Fig. 2 in Shi and Durran (2014)], and we believe it may contribute to differences in rain-shadow strength among real-world mountain ranges as well—for example, between the Sierra Nevada and the Cascades. However, the extent to which rain-shadow differences can be attributed to latitude—versus, for example, topography—remains an open question.

Our results may also have implications for how midlatitude mountain ranges will be affected by future climate change. For example, if midlatitude storm tracks shift poleward as predicted (e.g., Yin 2005), many locations might be expected to experience a decrease in the fraction of precipitation associated with warm fronts. Based on our analysis above, this could result in a widespread increase in the strength of the rain shadow in mountain ranges downwind of the major storm tracks, such as the Cascades, the southern Andes, and the Southern Alps. This effect will have to be considered alongside a number of other factors when considering the impact of climate change on precipitation in any particular mountain range (e.g., Siler and Roe 2014; Pavelsky et al. 2012; Shi and Durran 2014).

Acknowledgments. We thank Gerard Roe for helpful discussions over the course of this project, Beth Tully for her assistance with Fig. 18, and Justin Minder for a very thorough and insightful review. We also acknowledge high-performance computing support from Yellowstone (ark:/85065/d7wd3xhc) provided by NCAR's Computational and Information Systems Laboratory, sponsored by the National Science Foundation. This work was supported by National Science Foundation Grants AGS-1138977 and AGS-1545927.

APPENDIX

A Moisture-Budget Method for Calculating the Flux across the Crest

The net transport of water vapor across the Cascade crest is given by

$$F_{\text{crest}} = \frac{1}{g}\int_C \left[\int_0^{p_s} (q\mathbf{u}\cdot\mathbf{r})\,dp\right] dC, \qquad \text{(A1)}$$

where $\int_C$ represents the line integral along the crest, g is standard gravity, q is the specific humidity, $\mathbf{u}$ is the vector horizontal wind, $\mathbf{r}$ is the unit vector normal to the crest in the horizontal plane, p is the vertical pressure coordinate, and p_s is the surface pressure. Unfortunately, while Eq. (A1) is straightforward in principle, it is difficult to evaluate numerically because of the complex geometry of the crest.

A simpler and more accurate approach is to solve for F_{crest} within the regional water-vapor budget. Let us define $\overline{q}$ as the total mass of atmospheric water vapor within a given region and $\overline{S}$ as the rate at which water vapor is being generated in the same region as a result of phase changes in the atmosphere and evaporation from the surface. The rate of change of $\overline{q}$ in the region is then given by

$$\frac{d\overline{q}}{dt} = \overline{S} - \iiint_V (\nabla\cdot F_q)\,dV, \qquad \text{(A2)}$$

where the last term represents the divergence of the water-vapor flux F_q from the volume V which encloses the region. From the divergence theorem, this term is equivalent to

$$\iiint_V (\nabla\cdot F_q)\,dV = \frac{1}{g}\oint_R \left[\int_0^{p_s} (q\mathbf{u}\cdot\mathbf{r})\,dp\right] dR, \qquad \text{(A3)}$$

where $\oint_R$ is the line integral along the entire boundary of the region and $\mathbf{u}$, $\mathbf{r}$, and q are defined as in Eq. (A1).

We can use Eqs. (A2) and (A3) to solve for F_{crest} as follows. First, we estimate $d\overline{q}/dt$ by calculating the change in total water vapor in the region west of the Cascades over the 6-h period of maximum precipitation for each storm. We then calculate $\overline{S}$ as the total rate of surface evaporation minus atmospheric condensation in the same region, averaged over the same period. From Eq. (A2), $\overline{S} - d\overline{q}/dt$ is equal to the net divergence of water vapor from the region.

To find F_{crest} from this divergence term, we must first calculate the net transport of water vapor out of the region through the northern, western, and southern boundaries (dashed black lines in Figs. 4 and 5). This step is conceptually equivalent to evaluating the line integral in Eq. (A1), but with the crest replaced by the much simpler geometry of the three other boundaries. Subtracting this transport from the net divergence gives F_{crest}.

To confirm the accuracy of this method, we performed the same calculation over the eastern slopes, where the transport across the crest represents a convergence term in the water-vapor budget. For each storm, the west-slope and east-slope results differed by no more than 3%, giving us high confidence in the accuracy of the method. The values in the second column of Table 2 reflect the average of the two estimates. The same method was also used to calculate the flux of condensate across the crest (third column of Table 2), with S given by the rate of atmospheric condensation minus precipitation at the surface.

REFERENCES

Durran, D. R., and J. B. Klemp, 1983: A compressible model for the simulation of moist mountain waves. *Mon. Wea. Rev.*, **111**, 2341–2361, doi:10.1175/1520-0493(1983)111<2341:ACMFTS>2.0.CO;2.

Gaberšek, S., and D. R. Durran, 2006: Gap flows through idealized topography. Part II: Effects of rotation and surface friction. *J. Atmos. Sci.*, **63**, 2720–2739, doi:10.1175/JAS3786.1.

Hong, S.-Y., 2010: A new stable boundary-layer mixing scheme and its impact on the simulated East Asian summer monsoon. *Quart. J. Roy Meteor. Soc.*, **136**, 1481–1496, doi:10.1002/qj.665.

Lee, T. J., R. A. Pielke, R. C. Kessler, and J. Weaver, 1989: Influence of cold pools downstream of mountain barriers on downslope winds and flushing. *Mon. Wea. Rev.*, **117**, 2041–2058, doi:10.1175/1520-0493(1989)117<2041:IOCPDO>2.0.CO;2.

Leung, L. R., Y. Qian, X. Bian, W. M. Washington, J. Han, and J. O. Roads, 2004: Mid-century ensemble regional climate change scenarios for the western United States. *Climatic Change*, **62**, 75–113, doi:10.1023/B:CLIM.0000013692.50640.55.

Mass, C., N. Johnson, M. Warner, and R. Vargas, 2015: Synoptic control of cross-barrier precipitation ratios for the Cascade Mountains. *J. Hydrometeor.*, **16**, 1014–1028, doi:10.1175/JHM-D-14-0149.1.

Niu, G.-Y., and Coauthors, 2011: The community Noah land surface model with multiparameterization options (Noah-MP): 1. Model description and evaluation with local-scale measurements. *J. Geophys. Res.*, **116**, D12109, doi:10.1029/2010JD015139.

Pavelsky, T. M., S. Sobolowski, S. B. Kapnick, and J. B. Barnes, 2012: Changes in orographic precipitation patterns caused by a shift from snow to rain. *Geophys. Res. Lett.*, **39**, L18706, doi:10.1029/2012GL052741.

Shi, X., and D. R. Durran, 2014: The response of orographic precipitation over idealized midlatitude mountains due to global increases in CO_2. *J. Climate*, **27**, 3938–3956, doi:10.1175/JCLI-D-13-00460.1.

Siler, N., and G. Roe, 2014: How will orographic precipitation respond to surface warming? An idealized thermodynamic perspective. *Geophys. Res. Lett.*, **41**, 2606–2613, doi:10.1002/2013GL059095.

——, and D. Durran, 2015: Assessing the impact of the tropopause on mountain waves and orographic precipitation using linear theory and numerical simulations. *J. Atmos. Sci.*, **72**, 803–820, doi:10.1175/JAS-D-14-0200.1.

——, G. Roe, and D. Durran, 2013: On the dynamical causes of variability in the rain-shadow effect: A case study of the Washington Cascades. *J. Hydrometeor.*, **14**, 122–139, doi:10.1175/JHM-D-12-045.1.

Smith, R. B., 2006: Progress on the theory of orographic precipitation. *Geol. Soc. Amer. Spec. Pap.*, **398**, 1–16, doi:10.1130/2006.2398(01).

Thompson, G., P. R. Field, R. M. Rasmussen, and W. D. Hall, 2008: Explicit forecasts of winter precipitation using an improved bulk microphysics scheme. Part II: Implementation of a new snow parameterization. *Mon. Wea. Rev.*, **136**, 5095–5115, doi:10.1175/2008MWR2387.1.

Yin, J. H., 2005: A consistent poleward shift of the storm tracks in simulations of 21st century climate. *Geophys. Res. Lett.*, **32**, L18701, doi:10.1029/2005GL023684.

Zängl, G., 2005: The impact of lee-side stratification on the spatial distribution of orographic precipitation. *Quart. J. Roy. Meteor. Soc.*, **131**, 1075–1091, doi:10.1256/qj.04.118.

——, and M. Hornsteiner, 2007: The exceptional Alpine south foehn event of 14–16 November 2002: A case study. *Meteor. Atmos. Phys.*, **98**, 217–238, doi:10.1007/s00703-006-0257-9.

Zhang, D., and R. A. Anthes, 1982: A high-resolution model of the planetary boundary layer—Sensitivity tests and comparisons with SESAME-79 data. *J. Appl. Meteor.*, **21**, 1594–1609, doi:10.1175/1520-0450(1982)021<1594:AHRMOT>2.0.CO;2.